

## Solar energy trapping with modulated silicon nanowire photonic crystals

Guillaume Demésy and Sajeev John

Citation: *J. Appl. Phys.* **112**, 074326 (2012); doi: 10.1063/1.4752775

View online: <http://dx.doi.org/10.1063/1.4752775>

View Table of Contents: <http://jap.aip.org/resource/1/JAPIAU/v112/i7>

Published by the [American Institute of Physics](#).

---

### Related Articles

Solar power conversion efficiency in modulated silicon nanowire photonic crystals  
*J. Appl. Phys.* **112**, 074327 (2012)

Hybrid pentacene/a-silicon solar cells utilizing multiple carrier generation via singlet exciton fission  
*Appl. Phys. Lett.* **101**, 153507 (2012)

Light trapping in solar cells: Analytical modeling  
*Appl. Phys. Lett.* **101**, 151105 (2012)

Performance of p- and n-side illuminated microcrystalline silicon solar cells following 2MeV electron bombardment  
*Appl. Phys. Lett.* **101**, 143903 (2012)

Light trapping enhancements of inverted pyramidal structures with the tips for silicon solar cells  
*Appl. Phys. Lett.* **101**, 141113 (2012)

---

### Additional information on *J. Appl. Phys.*

Journal Homepage: <http://jap.aip.org/>

Journal Information: [http://jap.aip.org/about/about\\_the\\_journal](http://jap.aip.org/about/about_the_journal)

Top downloads: [http://jap.aip.org/features/most\\_downloaded](http://jap.aip.org/features/most_downloaded)

Information for Authors: <http://jap.aip.org/authors>

## ADVERTISEMENT



Special Topic Section:  
**PHYSICS OF CANCER**

Why cancer? Why physics? [View Articles Now](#)

# Solar energy trapping with modulated silicon nanowire photonic crystals

Guillaume Demésy<sup>a)</sup> and Sajeev John

*Department of Physics, University of Toronto, 60 St. George Street, Toronto, Ontario M5S 1A7, Canada*

(Received 1 February 2012; accepted 17 July 2012; published online 12 October 2012)

We demonstrate the efficacy of nanostructured thin film silicon solar cells to trap and absorb approximately 75% of all sunlight incident (400 nm–1200 nm) with an equivalent bulk thickness of only 1 micron of silicon. This is achieved by sculpting the collection zone into a three-dimensional, simple-cubic-symmetry, photonic crystal consisting of modulated silicon nanowires embedded in SiO<sub>2</sub> and sitting on a quartz substrate with no metallic mirrors. A specific modulation of the radius of nanowires provides antireflection, strong light trapping, and back-reflection mechanisms in targeted spectral regions. This modulation is linear at the top of the nano-rods leading to nanocones at the solar cell to air boundary. These silicon nanocones are very good absorbers at short wavelengths and act as broadband coupler to a light-trapping region below at longer wavelengths. In the light trapping region the modulation is periodic to form a simple cubic photonic crystal exhibiting a broad spectrum of strong parallel interface refraction resonances. Here, light incident from most angles is deflected into slow group velocity modes with energy flow nearly parallel to the interface, long dwell times, and strong light intensity enhancement (up to 150 times the incident intensity) in specific regions. Finally, a stronger and chirped modulation of the nanowire underneath provides back-reflection by means of a one-dimensional depth-dependent photonic stop-gap. The possibility of absorbing light at energies below the electronic band gap of silicon is illustrated using a graded index Si<sub>x</sub>Ge<sub>1-x</sub> alloy in the bottom section of each nanowire. Each nanowire is amenable to a radial P-N junction for proximal charge carrier separation and efficient collection of photo-generated current. © 2012 American Institute of Physics. [<http://dx.doi.org/10.1063/1.4752775>]

## I. INTRODUCTION

Photovoltaic devices that turn sunlight directly into electricity offer a competitive and limitless source of energy provided that their light capture and conversion efficiencies can be improved while using a small amount of semi-conductor material. The earth receives solar radiation of up to  $1.7 \times 10^{17}$  W in the upper atmosphere<sup>1</sup> whereas the rate of current worldwide energy consumption is about 10 000 times smaller at  $\sim 1.6 \times 10^{13}$  W. However, nearly half of the cost of fabrication of the so-called first generation of solar cell modules currently used comes from the silicon wafer itself.<sup>2,3</sup> These first generation solar cells require bulk semi-conductor slabs, a few hundreds microns thick, and provide power conversion or external quantum efficiency (EQE) of roughly 10%. A second generation already exists in which the costly semiconductor medium is textured into thin films, with substantially reduced costs but generally a lower EQE.<sup>4</sup> This poor solar power utilization stems from our inability to optically control a sequence of light harnessing processes: solar collection, solar absorption, and solar spectral bandwidth utilization.

While silicon is a promising photovoltaic material for its long term reliability, natural abundance, and compatible electronic band gap, the indirect nature of this band gap makes long wavelength absorption problematic in thin films.

The dispersion properties of crystalline silicon imply a broad range of absorption lengths (depicted in black in Fig. (1)) ranging from 10 nm at a wavelength of 400 nm to almost 1 cm at a wavelength of 1.1  $\mu$ m. Four different

spectral windows in the solar spectrum received on earth are highlighted Fig. (1). In the bluish region ( $\lambda < 450$  nm), electron-hole pairs are generated very close to the surface, which can lead to enhanced radiative recombination before collection. The greenish region ( $450 \text{ nm} < \lambda < 800$  nm) corresponds to a charge carrier generation in the volume of the silicon. Some fraction of these carriers is lost through non-radiative Auger and Shockley-Read-Hall recombinations. In the reddish region ( $800 \text{ nm} < \lambda < 1200$  nm), the absorption length in silicon is very long, and several hundreds of microns in bulk thickness are needed for substantial carrier generation. However, if these carriers are generated too far from the P-N junction, where charge separation occurs, they will likely be lost due to recombination. A challenge common to all three spectral windows above arise from the fact that the photon energy is substantially greater than the electronic bandgap of silicon. Roughly one-third of available solar power is lost when so-called *hot carriers* lose energy by thermalization<sup>5</sup> and drop to the energy of the electronic band gap of silicon. This occurs by interaction with phonons and on the time scale of tens of picoseconds after carrier generation. This thermalization loss is particularly significant for very energetic photons of the bluish region of Fig. (1). A major improvement in solar cell efficiency could be achieved if carriers generated by these photons can be separated and collected before complete relaxation to the electronic band edge states.<sup>6,7</sup> Nano-structured photonic crystals can considerably reduce the time scale between carrier generation and collection. Finally the white region ( $\lambda > 1200$  nm) in Fig. (1) corresponds to photons of lower energy than the silicon band gap and requires a spectral re-shaping through nonlinear

<sup>a)</sup>Electronic mail: [gdemesy@physics.utoronto.ca](mailto:gdemesy@physics.utoronto.ca).

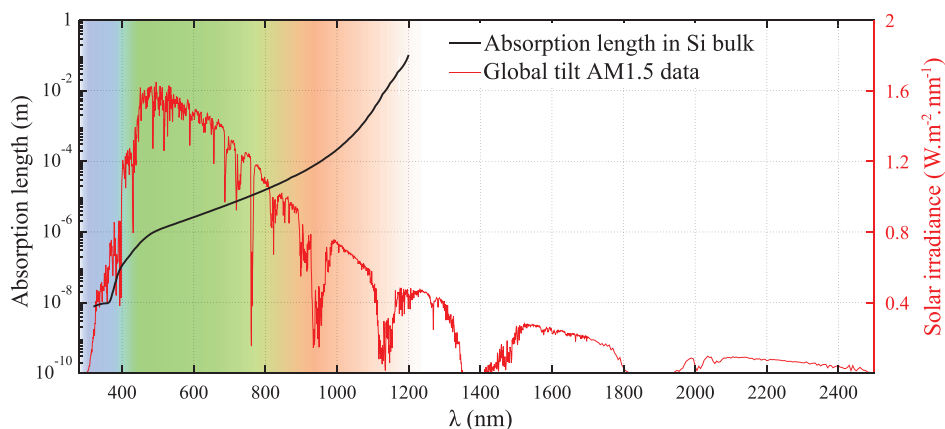


FIG. 1. Spectral irradiance AM1.5 of the sun incident on the surface of earth (global tilt<sup>40</sup>, in red) and absorption length (in black) of crystalline silicon.<sup>41</sup> The colored background highlights issues peculiar to each spectral regions. The bluish region corresponds to very energetic photons that suffer strong losses due to thermalization. The greenish region corresponds to the peak of solar emission. The absorption in the cell should be as strong as possible while the absorption length in silicon increases exponentially. In the reddish region, the absorption length exceeds  $100\ \mu\text{m}$  and a strong light trapping mechanism is essential. The white region corresponds to photons with energy below the band gap of crystalline silicon. In order to address this spectral window, nonlinear spectral conversion mechanisms and/or other semi-conductor materials of lower band gap, such as germanium, should be considered.

processes such as photon up-conversion<sup>8–10</sup> or the use of another semiconductor of lower electronic band gap.

From a purely optics perspective, a significant factor in the inefficiency, if conventional silicon-based solar energy conversion devices, is their inability to trap incoming photons from the sun over a broad range of incident angles and a broad range of incident frequencies. In conventional silicon thin films the majority of incident sunlight is transmitted or reflected rather than absorbed. While specific structuring of thin films can provide resonant absorption at specific frequencies and specific incident angles,<sup>11</sup> a simple, broadband, wide-acceptance-angle thin-film architecture has yet to be implemented for light trapping and solar energy harvesting. Photonic crystal (PC) materials are periodic nano-structured dielectric materials with engineered periodicity in the range of one-third to one-half the wavelength of light. The most fundamental property of PC materials is their ability to trap and localize light.<sup>12,13</sup> They also enable redistribution of the electromagnetic density of states (DOS). While PCs are often associated with the creation of a complete band gap, they can also provide significant enhancements of the photonic DOS in spectral ranges of importance to optical absorption. Such enhancements are often associated with modes exhibiting slow group velocities and long optical dwell times, leading to absorption even when the intrinsic absorption length scale of the bulk material is very long. Moreover, it is possible to engineer the refractive coupling between external plane waves and modes in enhanced photonic DOS. The Bloch nature of electromagnetic modes in the PC enables strong focussing of light intensity in specific regions where absorption or nonlinear response are desired. PC materials offer new and unexplored avenues to address the fundamental issues of photon management and electron management detailed above. PC architectures enable entirely new degrees of freedom to tailor the behavior of the solar cell to the solar spectrum as well as embed charge separation and collection structures in novel ways to circumvent electronic loss mechanisms.

The idea of periodically structured matter in solar cells has been considered in the recent literature. 1D,<sup>14,15</sup> 2D,<sup>15–17</sup>

and more recently 3D<sup>18–20</sup> structures have been proposed. These consist of diffraction gratings to improve the air-to-solar cell coupling (antireflective) or improve the confinement of light inside the solar cell (back-reflector). Patterning the light absorbing region of the solar cell itself has also been considered. Mallick *et al.*<sup>21</sup> proposed a 3D structuring of the active region, providing improvement of the optical absorption compared to an unstructured bulk material. Their structure is 2D photonic crystal of stacked nano-holes of two different diameters together with metallic a back reflector.

Another promising architecture is the silicon nanowire array.<sup>23,24</sup> Several recent experimental realizations<sup>25–28</sup> have shown reasonable agreement with numerical simulation of optical reflection and transmission.<sup>29,30</sup> These architectures offer more proximal collection of generated charges inside the absorber by a radial construction of the P-N junction around the nanowire. However, neither optimization of 2D photonic crystal properties of existing nanowire arrays nor patterning in the third dimension has been considered.

In this paper, we propose and demonstrate the efficacy of modulated silicon nanowires that form 3D simple cubic photonic crystals in order to exhibit better solar absorption than their straight counterparts. This is largely achieved through a sinusoidal modulation in radius of the middle section of the nanowires that leads to a three-dimensional (3D) simple cubic (SC) photonic crystal. This photonic crystal has enhanced electromagnetic density of states in targeted parts of the solar spectrum. The relevant electromagnetic modes exhibit a slow group velocity and act as a continuous spectral distribution of high quality optical resonances with strong light focussing in specific regions of the modulated nano-rod PC. Coupling of sunlight from nearly any incident angle occurs through the phenomenon of parallel-to-interface (negative) refraction (PIR).<sup>31</sup> This leads to a long dwell time for light for a thin film structure even in a spectral range where the intrinsic absorption of silicon is weak. The top section of each nanowire is tapered in the form of a cone to provide an effective graded average refractive index for incoming light. The bottom section of each nanowire is

modulated so as to provide a one dimensional photonic crystal back-reflector whose reflection spectrum is continuously red-shifted as light propagates deeper within the nano-structure. A first set of modulation parameters is shown to provide better absorption properties than any straight 2D nanowire photonic crystal of the same equivalent bulk thickness of silicon. A second set of modulation parameters, applied to the base section of each nanowire, is shown to provide back-reflection of light not already absorbed in the upper two sections of the nano-rods. Unlike a conventional metallic mirror, our dielectric back-reflector is part of the active region of the solar cell and contributes considerably to the photo-generated currents. Finally, we show that a nearly 25% enhancement in photo-current can be obtained by means of a compositional modulation of the form  $\text{Si}_x\text{Ge}_{1-x}$ , where  $x$  varies linearly from zero at the top of the base section to unity at the bottom.

## II. SOLAR ABSORPTION IN THE WAVE OPTICS REGIME

### A. Maxwell's equations in a thin film photonic crystal

When light impinges on a photonic crystal solar cell consisting of a three-dimensional nano-structure with feature sizes and periodicity less than the optical wavelength, Maxwell's equations must be numerically solved in their general vector form. This wave optics regime offers new opportunities for efficient light harvesting not found in the first generation of photovoltaic cells consisting of a simple silicon bulk material operating in the ray optics regime, where the simplest form of the Snell-Descartes law applies. We consider 3D photonic crystal slabs as depicted in Fig. 2, with lattice constants  $a_x$ ,  $a_y$ , and  $a_z$  in the respective  $x$ ,  $y$ , and  $z$ -directions. An incident plane wave with time dependence  $\exp(-i\omega t)$  is described by the following field amplitude

$$\mathbf{E}_0 = \mathbf{A}_0 \exp(i\mathbf{k}_0 \cdot \mathbf{r}). \quad (1)$$

Here, the wave vector is denoted  $\mathbf{k}_0 = [k_{0x}, k_{0y}, k_{0z}] = [-\sin\theta_0 \cos\varphi_0, -\sin\theta_0 \sin\varphi_0, -\cos\theta_0]$  and the amplitude  $\mathbf{A}_0 = [E_x^0, E_y^0, E_z^0] = E_0 [\cos\psi_0 \cos\theta_0 \cos\varphi_0 - \sin\psi_0 \sin\varphi_0, \cos\psi_0 \cos\theta_0 \sin\varphi_0 + \sin\psi_0 \cos\varphi_0, -\cos\psi_0 \sin\theta_0]$ , where  $\varphi_0 \in [0, 2\pi]$ ,  $\theta_0 \in [0, \pi/2]$  and  $\psi_0 \in [-\pi/2, \pi/2]$ . The polarization angle  $\psi_0$  is equal to 0 (resp.  $\pi/2$ ) in the  $p$ -polarization (resp.  $s$ -polarization) case. The solar spectrum shown in Fig. 1 consists of an infinite superposition of plane waves of wavelength  $\lambda_0$  ranging from 270 nm to  $2.5\mu\text{m}$ , wave-vectors with  $k_{0z} < 0$ , and all possible polarization angles.

The problem of optical diffraction and absorption corresponds to solving Maxwell's equations for the electric and magnetic fields ( $\mathbf{E}$ ,  $\mathbf{H}$ ) of fixed frequency  $\omega$

$$\begin{cases} \text{curl } \mathbf{E} = i\omega \mu_0 \mu \mathbf{H} \\ \text{curl } \mathbf{H} = -i\omega \varepsilon_0 \varepsilon(\mathbf{r}, \omega) \mathbf{E}, \end{cases} \quad (2a) \quad (2b)$$

such that the diffracted field satisfies an outgoing waves condition and where  $\mathbf{E}$  and  $\mathbf{H}$  are quasi-bi-periodic functions with respect to  $x$  and  $y$  coordinates.<sup>32</sup> Here  $\varepsilon_0$  and  $\mu_0$  are the permittivity and permeability of free space.  $\varepsilon(\mathbf{r}, \omega)$

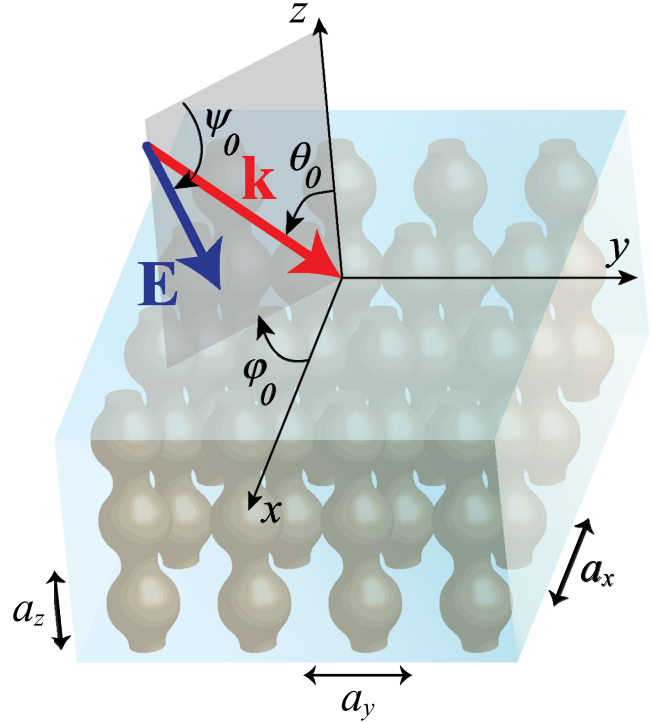


FIG. 2. Three dimensional simple cubic photonic crystal slabs have finite thickness in  $z$ -direction but are infinite along  $Ox$  and  $Oy$ , with lattice constants are denoted  $a_z$ ,  $a_x$ , and  $a_y$ . The three cells-thick photonic crystal made of modulated nanowires exhibits parallel to interface refraction (PIR). The incident solar spectrum can be sampled into an infinite superposition of incoherent linearly polarized plane waves of wave-vectors defined by the angles  $\theta_0$  with respect to the  $z$ -axis,  $\varphi_0$  in the  $x$ - $y$  plane and of polarization angle (between plane of incidence, in dark gray, and the electric field)  $\psi_0$ .

is the frequency dependent, spatially periodic dielectric function of the thin film solar cell and surrounding medium. It has both a real and imaginary part but is assumed not to depend on the intensity of the incident light. Since we consider nonmagnetic materials, we set  $\mu = 1$ . The field diffracted by the photonic crystal slab can be obtained using an appropriate formulation of the finite element method (FEM) as detailed in Refs. 33 and 34. In comparison with the more commonly used finite-difference time-domain (FDTD) method,<sup>35</sup> FEM using tetrahedral unstructured volume mesh is well suited to the modelling of objects with arbitrary curved surfaces and oblique incidences. FDTD methods, developed for these purposes, include subpixel smoothing<sup>36</sup> and an iterative technique for oblique incidence.<sup>37</sup> FEM in frequency domain readily takes into account the dispersion of materials. We note that a modified Lorentz approximation could alternatively be employed to model the silicon dielectric function at 300–1000 nm range in FDTD.<sup>38</sup>

Quantities relevant to solar energy harvesting are calculated as follows. Normalized absorption  $\alpha_s$  in the semiconductor can be obtained through the computation of the following ratio:

$$\alpha_s(\lambda, \theta_0, \varphi_0, \psi_0) = \frac{\int_{V_s} \omega \varepsilon_0 \Im m(\varepsilon^s) |\mathbf{E}|^2 dx dy dz}{\int_S \Re e\{\mathbf{E}_0 \times \mathbf{H}_0^*\} \cdot \mathbf{n} dx dy}. \quad (3)$$

Here, the subscript,  $s$ , denotes that we only include absorption within the silicon and the superscript,  $*$ , represents the complex conjugate. The numerator in Eq. (3) describes absorption in watts per unit cell area of the photonic crystal and is computed by integrating the absorption density over the volume  $V_s$  of silicon inside one 2D-unit cell of the 3D thin film photonic crystal with complex isotropic dielectric constant  $\epsilon^s$ . The denominator normalizes this absorbed power to the incident power, i.e., the time-averaged incident Poynting vector flux across the top surface of one 2-D unit cell (a rectangular surface  $S$  of area  $a_x a_y$  in the superstrate parallel to the  $x$ - $y$  plane, with normal  $\mathbf{n}$  oriented along decreasing values of  $z$ ). Since  $\mathbf{E}_0$  is simply the incident plane wave defined at Eq. (1), the denominator in Eq. (3) is equal to  $(E_0^2 \sqrt{\epsilon_0/\mu_0} a_x a_y)/\cos(\theta_0)$ .

We denote by  $\mathbf{E}_{\text{inc}}$  (resp.  $\mathbf{H}_{\text{inc}}$ ) the restriction of  $\mathbf{E}_0$  (resp.  $\mathbf{H}_0$ ) to the free space (air) superstrate, and  $\mathbf{E}_d = \mathbf{E} - \mathbf{E}_{\text{inc}}$  (resp.  $\mathbf{H}_d = \mathbf{H} - \mathbf{H}_{\text{inc}}$ ) is the so-called diffracted electric (resp. magnetic) field. Reflection and transmission coefficients  $r$  and  $t$  are obtained from the field maps through the computation of the real part of the time-averaged Poynting vector as follows:

$$r(\lambda, \theta_0, \varphi_0, \psi_0) = \frac{\int_{S_{\text{sup}}} -\Re\{\mathbf{E}_d \times \mathbf{H}_d^*\} \cdot \mathbf{n} \, dx \, dy}{\int_S \Re\{\mathbf{E}_0 \times \mathbf{H}_0^*\} \cdot \mathbf{n} \, dx \, dy}, \quad (4a)$$

$$t(\lambda, \theta_0, \varphi_0, \psi_0) = \frac{\int_{S_{\text{sub}}} \Re\{\mathbf{E}_d \times \mathbf{H}_d^*\} \cdot \mathbf{n} \, dx \, dy}{\int_S \Re\{\mathbf{E}_0 \times \mathbf{H}_0^*\} \cdot \mathbf{n} \, dx \, dy}. \quad (4b)$$

Here  $S_{\text{sup}}$  (resp.  $S_{\text{sub}}$ ) is a rectangular surface of area  $a_x a_y$  in the superstrate (resp. substrate) defining the top (resp. bottom) of the 2-D PC unit cell, whose normal,  $\mathbf{n}$ , is oriented along decreasing values of  $z$ . We emphasize that the self-consistency of our numerical scheme is guaranteed at each wavelength and incident angle since the reflection  $r(\lambda, \theta_0, \varphi_0, \psi_0)$  is calculated using cuts of the EM field in the superstrate. The transmission  $t(\lambda, \theta_0, \varphi_0, \psi_0)$  is calculated using cuts of the EM field in the substrate, whereas the absorption  $\alpha(\lambda, \theta_0, \varphi_0, \psi_0)$  is obtained by integration of the EM field values inside the interior absorbing regions of the photonic crystal. Therefore,  $r$ ,  $t$ , and  $\alpha$  are obtained independently, making use of the EM field values throughout the computation cell. Their sum is compared to unity as a final consistency check.

## B. Optical performance measures of solar cells

An important benchmark for the power efficiency of a solar cell is the Shockley-Queisser limit.<sup>39</sup> The assumptions for this limit are (i) perfect absorption of all sunlight energies above the semiconductor electronic band gap, i.e., each photon creates exactly one electron/hole pair, (ii) complete and instantaneous thermalization of these charge carriers so that each generated electron drops to the bottom of the semiconductor conduction band and each hole rises to the top of the valence band, (iii) perfect collection of carriers, and

(iv) radiative recombination is the only other loss mechanism. According to the so-called Shockley-Queisser detailed balance, a c-Si (band gap 1.124 eV at room temperature) idealized P-N junction under thermal equilibrium yields the following power distribution: (i) 20.4% of the available incident solar power contained in the spectral range [400 nm–4000 nm] is not absorbed in silicon since these photons have energy lower than the electronic band gap, (ii) 29.8% of the incident solar power is lost by thermalization of electrons generated by photons of energy higher than the band gap, leaving behind (iii) 49.8% of the incident solar power for potential conversion to electrical power. This value of 49.8% is then further decomposed into three channels: (i) 1.6% of the incident solar power is lost through radiative recombination, (ii) 14.3% of the incident solar power is lost because the voltage leading to the maximum output power of the cell is lower than the band gap energy divided by electron charge, leaving behind only (iii) 33.9% of the incident solar power to participate to the final output photocurrent. Under these simplified conditions, the maximum short circuit current  $J$  of the silicon solar cell is 42.3 mA/cm<sup>2</sup>. This energy balance takes into account the contribution of photons of energy over 1.124 eV, considering realistic solar data.<sup>40</sup>

Considering the solar spectrum as a superposition of plane waves of arbitrary wave vector and polarization, the short circuit current, under the Shockley-Queisser conditions, can be deduced from Eq. (3)

$$J_{\lambda_{\text{min}}}^{\lambda_{\text{max}}} = \int_0^{2\pi} \int_0^{2\pi} \int_{-\pi/2}^{\pi/2} \int_{\lambda_{\text{min}}}^{\lambda_{\text{max}}} \frac{e \lambda}{h c} I(\lambda, \theta_0, \varphi_0, \psi_0) \alpha_s(\lambda, \theta_0, \varphi_0, \psi_0) \, d\lambda \, d\theta_0 \, d\varphi_0 \, d\psi_0. \quad (5)$$

Here,  $e$  is the electron charge,  $I(\lambda)$  is the solar light intensity incident on the cell per unit area per unit wavelength per unit solid angle,  $h$  is Planck's constant, and  $c$  is the speed of light in vacuum. By dividing the incident intensity (energy per unit time per unit area) in Eq. (5) by the photon energy  $\frac{hc}{\lambda}$ , we obtain the number of photons absorbed per unit time per unit area. Assuming that each absorbed photon per unit time translates into a single electronic charge,  $e$ , collected per unit time, we obtain the short circuit current (Eq. (5)). Under these assumptions, this current  $J$  is sometimes called the maximum achievable photo-current density (MAPD) in the literature.<sup>21</sup> Most silicon-based designs are rather effective in the visible range, but their efficiency drops drastically above 750 nm. The superscript  $\lambda_{\text{max}}$  and subscript  $\lambda_{\text{min}}$  (wavelengths given in nm) in Eq. (5) permit us to analyze the contribution of a portion  $[\lambda_{\text{min}}, \lambda_{\text{max}}]$  of the spectrum to the overall  $J_{400}^{1100}$ .

One drawback in the calculation of the short circuit current (Eq. (5)) is the lack of angular information concerning the solar spectrum. The common reference solar measurements<sup>40</sup> are made with a detector that integrates the incident light power over all angles. Many solar cell performance tests are then based on collimating all of this solar power into a single beam at normal incidence to the cell. However, since a large amount of solar light arrives more than 45° off-normal incidence, the performance of the device at off-normal angles is important.

While earlier literature<sup>21,26,29</sup> considers performance based on all the solar power collimated into the normal direction and linearly polarized along one axis of the periodic structure, we extend the performance criterion to the case where all the solar power is collapsed into an off-normal wave-vector defined by the angles  $\theta_0$  and  $\varphi_0$  with polarization angle  $\psi_0$ . This leads us to define an angle-dependent short-circuit current  $J_{\lambda_{\min}}^{\lambda_{\max}}(\theta_0, \varphi_0, \psi_0)$ . We emphasize again that this definition of the short circuit current is valid only under the Shockley-Queisser conditions: one photon incident in the semiconductor material leads to the generation and collection of one electron-hole pair, i.e., considering infinite carrier mobility and neglecting all non-radiative recombination losses.

In reality, a portion of the total solar power in the band  $[\lambda_{\min}, \lambda_{\max}]$  is either transmitted through or reflected by the solar cell. This typically leads to power efficiencies considerably below the Shockley-Queisser limit. These fractions  $T_{\lambda_{\min}}^{\lambda_{\max}}(\theta_0, \varphi_0, \psi_0)$  and  $R_{\lambda_{\min}}^{\lambda_{\max}}(\theta_0, \varphi_0, \psi_0)$  are defined as

$$T_{\lambda_{\min}}^{\lambda_{\max}}(\theta_0, \varphi_0, \psi_0) = \frac{\int_{\lambda_{\min}}^{\lambda_{\max}} t(\lambda, \theta_0, \varphi_0, \psi_0) I(\lambda) d\lambda}{\int_{\lambda_{\min}}^{\lambda_{\max}} I(\lambda) d\lambda}, \quad (6a)$$

$$R_{\lambda_{\min}}^{\lambda_{\max}}(\theta_0, \varphi_0, \psi_0) = \frac{\int_{\lambda_{\min}}^{\lambda_{\max}} r(\lambda, \theta_0, \varphi_0, \psi_0) I(\lambda) d\lambda}{\int_{\lambda_{\min}}^{\lambda_{\max}} I(\lambda) d\lambda}. \quad (6b)$$

Indeed  $R_{\lambda_{\min}}^{\lambda_{\max}}$  corresponds to the fraction of incident solar energy contained in the spectral window  $[\lambda_{\min}, \lambda_{\max}]$  that is irreparably lost, while  $T_{\lambda_{\min}}^{\lambda_{\max}}$  corresponds to the fraction of incident energy transmitted to the substrate, which could potentially be harvested using a second cell placed in tandem below the first. Finally, we specify the source of numerical data used for the different materials. All dielectric constants in this paper are linearly interpolated between the tabulated values given in Ref. 41.

We now study the optical response of various solar cell architectures. The first step of our design consists of finding the most absorptive geometrical configuration of conventional unmodulated nanowires arranged in a 2D square lattice. We use this optimized 2D nanowire array (for a given equivalent bulk thickness of silicon) as a benchmark for evaluating more complex 3D nano-structures.

### III. 2D PHOTONIC CRYSTAL OF SILICON NANOWIRES

In recent numerical studies of silicon nanowires, Hu *et al.*<sup>29</sup> compared the response of silicon nanowires floating in free space. Lagos *et al.*<sup>30</sup> considered the effect of varying specific parameters (periodicity, silicon filling fraction, height of the rods). Both these studies used fixed rod thickness, resulting in different equivalent slab thicknesses of silicon from case to case. In other words, the volume of semiconductor material changed while the structural parameters varied. As a result, it was not possible to ascertain whether

the performance of the solar cell was improved due to the choice of geometrical parameters or due to the use of a larger amount of silicon.

In our model of a photovoltaic device, we consider modulated silicon nanowires fully embedded in a silica slab and resting on a quartz substrate. Although this additional packaging of the silicon photonic crystal in an SiO<sub>2</sub> background leads to further reflexion losses at the top surface of the solar cell, it provides mechanical stability and protection to the overall device. More importantly, our constitutive parameter analysis and optimization is performed using a fixed equivalent slab thickness of silicon. In other words, the actual mass of semi-conductor material used per unit area remains the same as we vary structural parameters. In this way, attention is focussed on the role of geometry and nano-structure in optimizing light trapping through changes in the electromagnetic density of states and wave guiding, rather than simply increasing the volume of absorbing material. Our study aims to identify optimum structures for overall solar light trapping and absorption using approximately one micron (or less) equivalent bulk thickness of silicon, with no metallic mirrors in the device.

In the case of a 2D PC consisting of straight-wall, cylindrical nano-rods, the variational parameters are the lattice,  $a$ , and the radius,  $r_0$ , of the rods, given here as a fraction of  $a$ . The variation of  $J_{400}^{\lambda_g}(0, 0, 0)$ ,  $J_{400}^{\lambda_g}(0, 45, 0)$ , and  $J_{400}^{\lambda_g}(0, 45, 90)$ , as defined Eqs. (3) and (5), with  $a$  and  $r_0$  are shown in Fig. (3). All data on the maps presented in Fig. (3) is obtained by spanning the spectral range [400 nm–1200 nm] in 3 nm steps using the FEM approach described in Sec. II. At constant equivalent slab thickness of silicon of 500 nm, the  $J_{400}^{\lambda_g}(0, 0, 0)$  of the considered array at normal incidence as a function of the lattice constant and the rod radius exhibits a maximum of 16.50 mA/cm<sup>2</sup>, as shown in Fig. 3(a). It is located at  $(a, r_0) = (450, 0.192)$ . For comparison, a 500 nm thick slab of bulk silicon on a quartz substrate leads to a short circuit current  $J_{400}^{\lambda_g}(0, 0, 0)$  of only 4.45 mA/cm<sup>2</sup>. These optimum structural parameters found at normal incidence are close to the optimum parameters obtained when considering the solar spectral density collapsed into a single angle of incidence/polarization  $(\theta_0, \varphi_0, \psi_0) = (45^\circ, 0^\circ, 0^\circ)$  as depicted in Figs. 3(b) and 3(c), i.e., in both  $p$  and  $s$ -polarization cases. Light trapping in this simple 2D photonic crystal arises from two effects. One is the deflection of incident light into partially transverse directions by the 2D diffraction grating structure. Light of a given incident wavevector  $\mathbf{k}_i$  is deflected (provided that energy is conserved) into direction  $\mathbf{k}_i + \mathbf{G}_{\parallel,n}$ , where  $\{\mathbf{G}_{\parallel,n}\}$  are the set of reciprocal lattice of the 2D PC. The second trapping effect is the result of Fabry-Perot resonances due to internal reflection of light at the PC-air interface and the PC-substrate interface. As  $a$  and  $r_0$  varied, for a fixed equivalent bulk thickness of silicon, the overall rod height (vertical thickness of a 2D PC layer) varies, and the nature of these resonances also changes. The same study is conducted for a different equivalent bulk slab thicknesses of 211 nm (Figs. 3(d) and 3(e)). The optimum set of parameter is now found to be  $(a, r_0) = (350, 0.233)$  and leads to a  $J_{400}^{\lambda_g}(0, 0, 0)$  of 11.76 mA/cm<sup>2</sup>. For comparison, a 211 nm thick slab of bulk

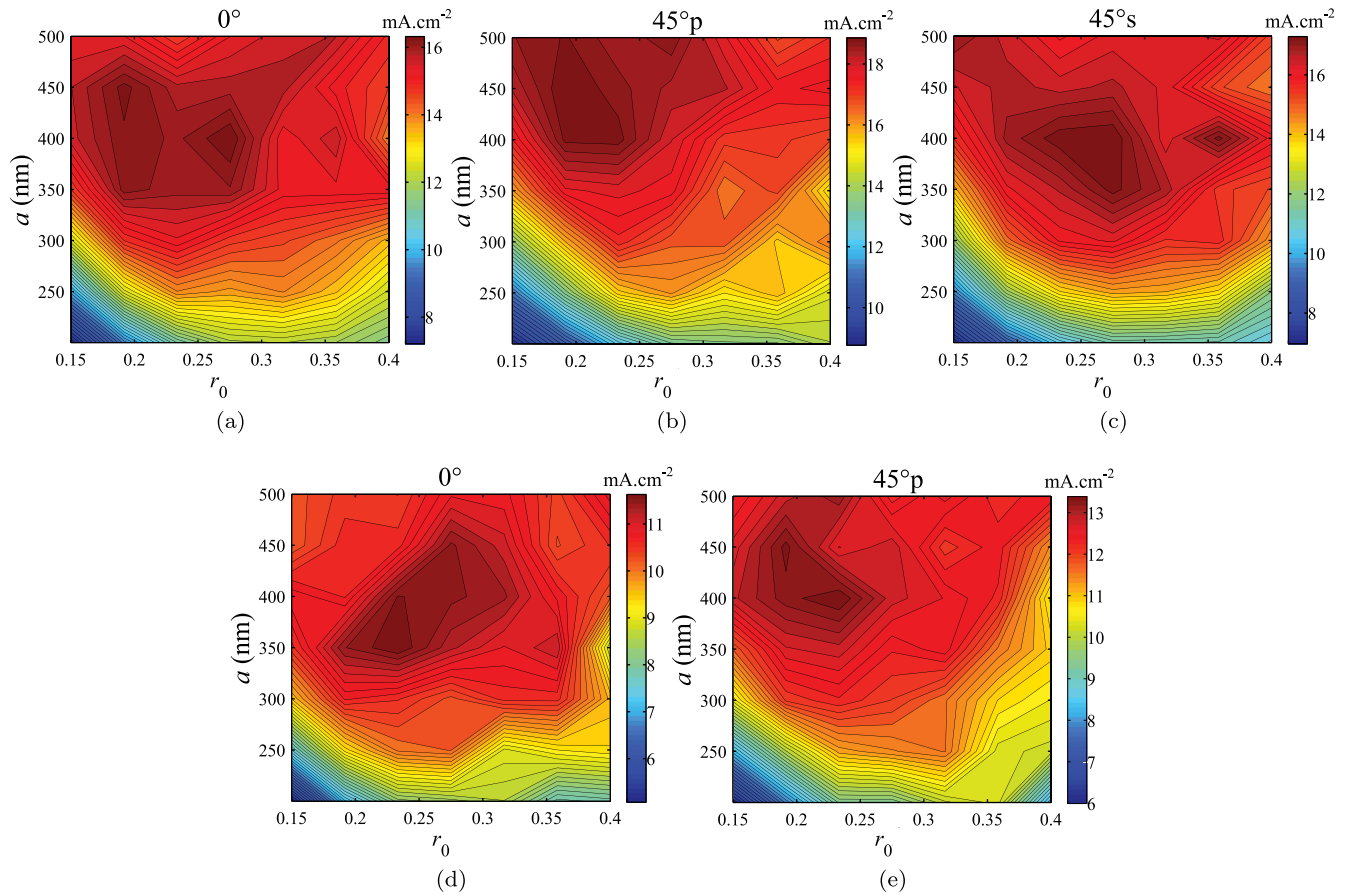


FIG. 3. Maximum achievable short circuit current  $J_{400}^{200}$  given in  $\text{mA}/\text{cm}^2$  of straight nanowires arrays as a function their structural parameters, radius  $r_0$  and periodicity  $a$ , for two different equivalent slab thicknesses, 500 nm and 211 nm. (a)–(c) 500 nm-equivalent slab thickness case, for different angles of incidence and polarization,  $(\theta_0, \phi_0, \psi_0) = (0^\circ, 0^\circ, 0^\circ), (45^\circ, 0^\circ, 0^\circ), (45^\circ, 0^\circ, 90^\circ)$ , respectively. (d),(e) 211 nm-equivalent slab thickness case, for different angles of incidence,  $(\theta_0, \phi_0, \psi_0) = (0^\circ, 0^\circ, 0^\circ), (45^\circ, 0^\circ, 0^\circ)$ , respectively. Nanowires arrays embedded in silica, with a lattice constant between 350 nm and 450 nm together with a radius  $r_0$  between 0.192 and 0.233 represent the optimal set of parameters for equivalent slab thicknesses between 200 nm and 500 nm.

silicon on a quartz substrate leads to a short circuit current  $J_{400}^{\lambda_{gs}}(0, 0, 0)$  of only  $3.57 \text{ mA}/\text{cm}^2$ .

In summary, for nanowires arrays, in the form of 2D square PC lattice, embedded in silica, placed on a quartz substrate, a lattice constant between 350 nm and 450 nm together with a radius between  $0.192a$  and  $0.233a$  provides

the optimal set of parameters for solar light absorption for an equivalent slab thickness of silicon between 200 nm and 500 nm. In what follows, we use the results of the optimized 2D photonic crystals as a benchmark to evaluate the performance of more sophisticated 3D photonic crystal designs.

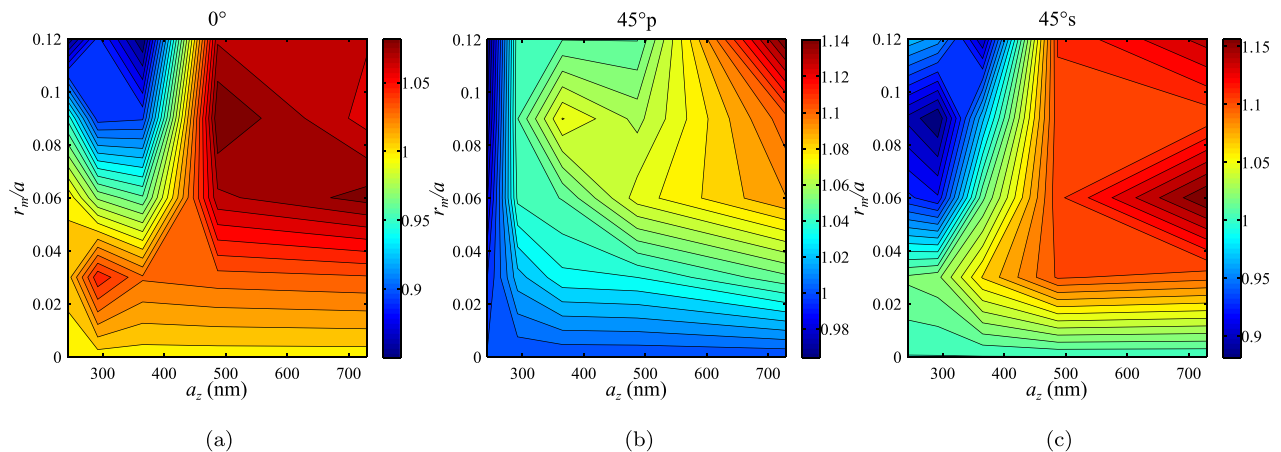


FIG. 4. Normalized maximum achievable short circuit current obtained with a sinusoidal modulation of the radius of the nanowires of the form  $a[r_0 + r_m \cos(2\pi z/a_z)]$ . The normalization is done with respect to the optimized straight nanowire case shown on Figs. 3(a)–3(c). The nanowires have an overall height close to  $3\mu\text{m}$ , periodicity  $a_x = a_y = a = 350 \text{ nm}$ , and radius  $r_0 = 0.233$ . The incident light directions and polarization are (a)  $(\theta_0, \phi_0, \psi_0) = (0^\circ, 0^\circ, 0^\circ)$ , (b)  $(\theta_0, \phi_0, \psi_0) = (45^\circ, 0^\circ, 0^\circ)$ , (c)  $(\theta_0, \phi_0, \psi_0) = (45^\circ, 0^\circ, 90^\circ)$ .

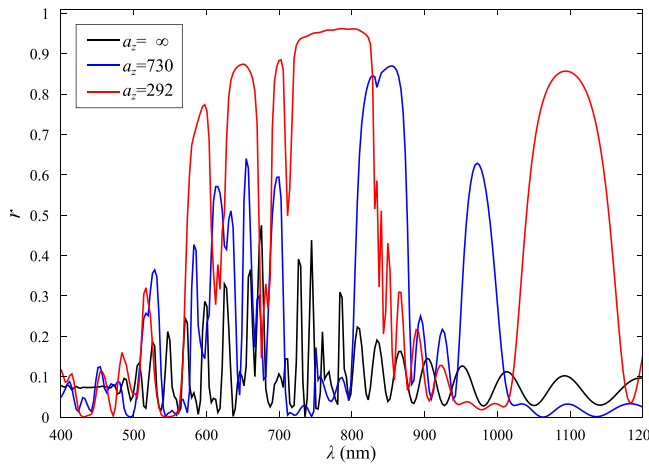


FIG. 5. Reflectivity  $r$  at normal incidence for  $(a, r_0, r_m) = (350, 0.233, 0.12)$  as the vertical periodicity of the modulation  $a_z$  decreases. Cases  $a_z \in \{\infty, 730, 292\}$  are represented in black, blue, and red, respectively.

#### IV. 3D PHOTONIC CRYSTALS OF MODULATED NANOWIRES

Strong light-trapping properties, together with more intense light concentration and slow group velocity effects, are available in three-dimensional photonic crystals. A simple sinusoidal modulation of the rods, forming a 3D photonic crystal with simple cubic symmetry, enhances the short circuit current of the square lattice nanowires array discussed in Sec. III. With the same amount of silicon, modulated nanowires have the ability to trap sunlight more effectively. We consider a modulation of the form  $a[r_0 + r_m \cos(2\pi z/a_z)]$  of the radius of each circular rod, where  $r_m$  and  $a_z$  are variational parameters. The resulting simple cubic PC has a lattice constant along the  $z$ -axis denoted  $a_z$ , while the amplitude of the modulation is denoted  $r_m$ . Fig. 4 shows the evolution of  $J_{400}^{\lambda_g}(0, 0, 0)$ ,  $J_{400}^{\lambda_g}(45, 0, 0)$ , and  $J_{400}^{\lambda_g}(45, 0, 90)$  as functions of  $a_z$  given in nanometers and  $r_m$  given as a fraction of the lattice constant  $a_x = a_y = a$ . The values of the color maps correspond to short circuit current normalized with respect to their optimized unmodulated counterparts of the same equivalent slab thickness of 500 nm (see Figs. 3(a)–3(c)). The flat

lines of constant  $J$  in the lower part of Figs. 4(a)–4(c) show the weak effect of a slight radial modulation. Indeed, the corresponding structures represent a slight modification of the nanowire topologies studied in Sec. III. For  $r_m \geq 0.06$  and  $a_z < 400$  nm, the nanowire modulation leads to an enhancement of the reflectivity of the structure due to the emergence of photonic stop gaps. This trend is particularly noticeable in the strong modulation  $r_m = 0.12$  case at normal incidence (dashed black line on Fig. 4(a)). Reflectivity  $r(\lambda, 0, 0, 0)$  and the overall reflection  $R_{400}^{1200}(0, 0, 0)$  as defined in Eq. (6) are shown for various structures in Fig. 5. While  $a_z$  decreases, keeping  $r_m = 0.12$  constant, the reflectivity peaks broaden and their amplitudes increase to nearly unity. This strong modulation leads to a drastic increase of the overall reflectivity of the nanowire array, making this choice of parameters unsuitable for the main solar absorber. A more moderate modulation, on the other hand, provides enhanced solar absorption due to light-trapping. Strong modulation is utilized in the base section of the nanowire, below the main solar absorber and (as shown in Sec. VI) serves as a dielectric back-reflector.

The photonic band diagrams for both the most reflecting configuration  $(a, a_z, r_0, r_m) = (350, 292, 0.233, 0.12)$  and the most absorbing configuration  $(a, a_z, r_0, r_m) = (350, 730, 0.233, 0.06)$  are shown in Fig. 6. They are calculated for the corresponding infinite photonic crystals along the edge of the first Brillouin zone using a finite element scheme.<sup>42</sup> These photonic band structures take into account the frequency dependence of the real part of the dielectric function of c-Si through the so-called cutting surface method.<sup>43</sup> Normalized frequencies higher than  $a/\lambda = 0.7$  ( $\lambda = 500$  nm) are not depicted since the corresponding absorption lengths become smaller than 3 lattice constants  $a$ . As shown in Fig. 7, the configuration  $(a, a_z, r_0, r_m) = (350, 730, 0.233, 0.06)$  offers a much higher density of electromagnetic modes to the incident plane wave than the configuration  $(a, a_z, r_0, r_m) = (350, 292, 0.233, 0.12)$ . The configuration  $(a, a_z, r_0, r_m) = (350, 730, 0.233, 0.06)$  leads to an improvement of the short circuit current  $J_{400}^{\lambda_g}$  of 8.5% at normal incidence and 16.6% (resp. 9.3%) at 45°-oblique incidence in the  $s$ - (resp  $p$ -)

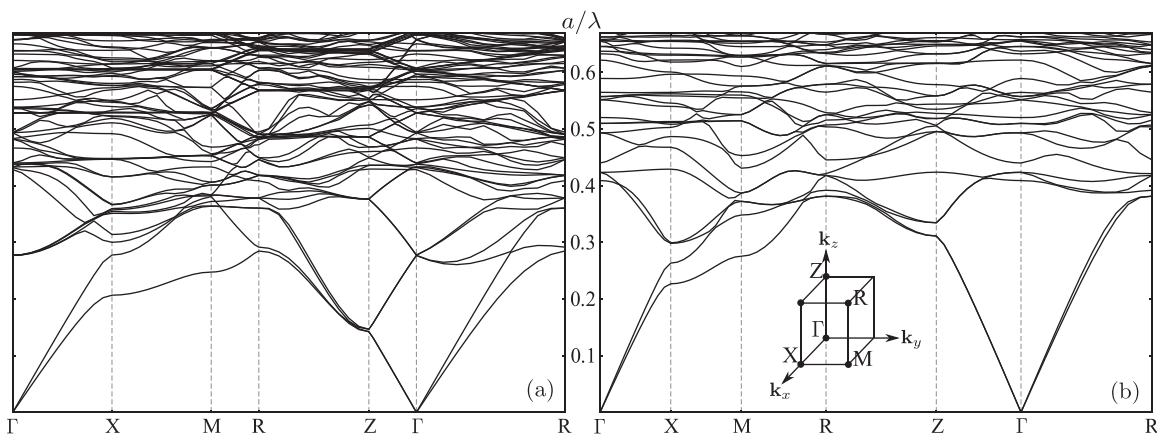


FIG. 6. Photonic band structure diagram of the 3D modulated silicon nanowires embedded in silicon dioxide with structural parameters (a)  $(a, a_z, r_0, r_m) = (350, 730, 0.233, 0.06)$  and (b)  $(a, a_z, r_0, r_m) = (350, 292, 0.233, 0.12)$ . The inset shows the first Brillouin zone and high-symmetry points at the zone boundary. The frequency dependence of the dielectric function of silicon is taken into account through a cutting surface method (CSM).<sup>43</sup>

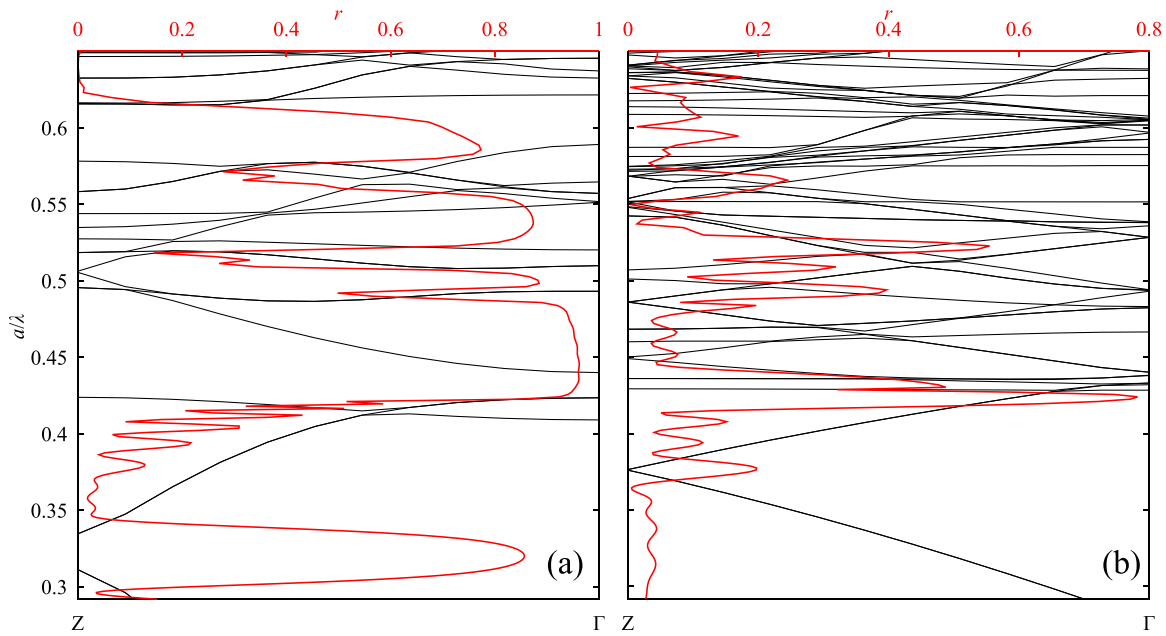


FIG. 7. Photonic band structure and reflectivity at normal incidence and reflectivity for the two nanowire configurations (a)  $(a, a_z, r_0, r_m) = (350, 730, 0.233, 0.06)$  and (b)  $(a, a_z, r_0, r_m) = (350, 292, 0.233, 0.12)$ .

polarization case compared to the optimized straight nanowire photonic crystal with the same equivalent bulk thickness of silicon.

The physical explanation for this enhancement depends on the spectral window. Consider the *p*-polarization case at oblique incidence  $\theta_0 = 45^\circ$ . In the visible range [400 nm, 750 nm], the contribution to the overall photocurrent  $J_{400}^{750}(45^\circ, 0, 0)$  is enhanced by a factor 9.4%. This occurs since the top of the modulated nanowire (MN), shaped as a truncated nanocone, enhances the absorption of light in the bluish part of spectrum. This is to be detailed in Sec. VII.

The most absorptive modulated nanowire structure consists of 4 vertical periods of a simple cubic photonic crystal. The frequency-dependent total electromagnetic DOS of this photonic crystal is depicted in red in Fig. 8(a). It is calculated using the iso-frequency surfaces in the first Brillouin zone of the first 50 photonic bands of the photonic crystal. The

dielectric dispersion of silicon is taken into account using the cutting surface method. The solid vertical bars in Fig. 8(a) indicate the spectral range covered by each of the fifteen first bands. The angular absorption spectrum  $\alpha(\lambda, \theta_0, 0, 0)$  of the four periods thick photonic crystal slab is presented in Fig. 8(b).

In the spectral range [400 nm–700 nm], the absorption of the MN slab remains very high for angles of incidence lower than  $30^\circ$ . The incident solar intensity is maximum over this range, and our 3D photonic crystal slab is designed with a high density of states to accommodate incoming sunlight at these wavelengths. Since the absorption length of silicon remains short in the visible range, the MN slab provides a good response in the visible range for any incident angle.

Above 750 nm, both the absorption and the DOS drop. However, multiple high absorption peaks as a function of frequency emerge at off-normal incidence, even for very

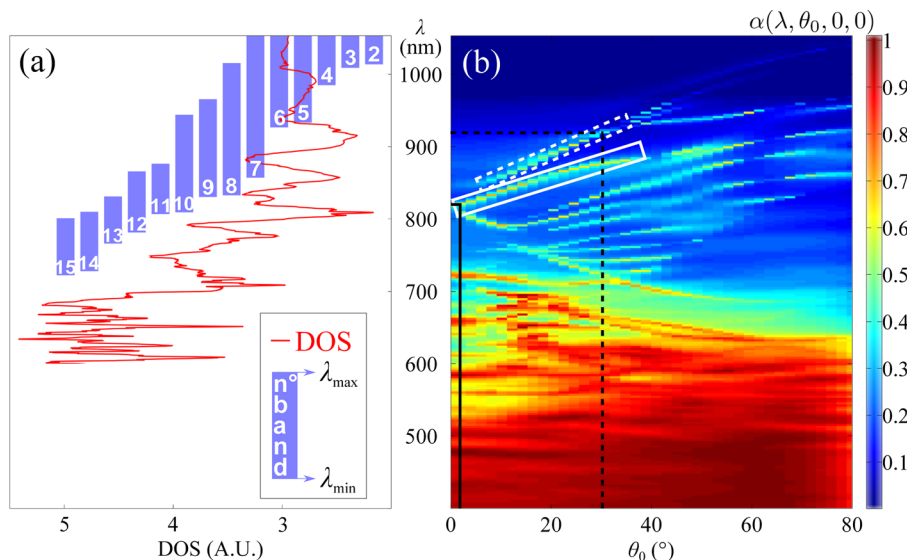


FIG. 8. (a) Total electromagnetic density of states of the infinite photonic crystal with nanowire parameters  $(a, a_z, r_0, r_m) = (350, 730, 0.233, 0.06)$ . (b) Optical absorption coefficient  $\alpha(\lambda, \theta_0, 0^\circ, 0^\circ)$  of a slab made of four unit cells in thickness for *p*-polarized incident sunlight.  $\alpha = 1$  (deep red) corresponds to 100% optical absorption. The silicon nanowires are embedded in  $\text{SiO}_2$  and the photonic crystal slab rests on a quartz substrate.

small values of  $\theta_0$ . This is due to the so-called PIR<sup>31</sup> from multiple photonic bands. Consider, for instance, the two elongated greenish streaks of Fig. 8(b) surrounded by white rectangular boxes. The streak surrounded by the plain (resp. dashed) rectangle is due to PIR from band 10 (resp. 7). PIR effect over a wide angular range arises when the surfaces of constant frequency in the electromagnetic dispersion  $\omega(\mathbf{k})$  are “flat” in the space of wave vectors  $\mathbf{k}$ . One property of simple cubic 3D photonic crystals is the prevalence of the flat iso-frequency surfaces, over a broad range of frequencies and wave-vectors, starting from the second or third photonic band and extending to higher frequencies. The overall iso-frequency surfaces may exhibit a cube-like shape, reflecting the underlying symmetry of the photonic crystal. To illustrate this, two particular  $\mathbf{k}$ -points, marked by the black lines in Fig. 8(b), are considered. The first  $\mathbf{k}$ -point  $(0.030 \frac{\pi}{a_x}, 0, 0.782 \frac{\pi}{a_z})$  corresponds to  $(\lambda, \theta_0, \varphi_0) = (819 \text{ nm}, 2^\circ, 0^\circ)$ , and the second  $\mathbf{k}$ -point  $(0.383 \frac{\pi}{a_x}, 0, 0.382 \frac{\pi}{a_z})$  corresponds to  $(\lambda, \theta_0, \varphi_0) = (918 \text{ nm}, 30^\circ, 0^\circ)$ . As depicted in Fig. 9(a) (resp. Fig. 9(b)), the iso-frequency surfaces of band 10 (resp. band 7) are very flat at both  $\mathbf{k}$ -points marked by the intersection of the two solid (resp. dashed) black lines. The propagation directions of these Bloch modes are given by

the direction of the group velocity at these Bloch vectors. Since the group velocity  $\mathbf{v}_g \equiv \nabla_{\mathbf{k}}$ , the direction of energy flow in the photonic crystal is perpendicular to the tangential surface of the iso-frequency surface. Due to the flatness of the iso-frequency surfaces, the direction of the group velocity is nearly parallel to the air/PC slab interfaces. Moreover, this group velocity in nearly flat dispersion bands  $\omega(\mathbf{k})$  is considerably less than that in a homogeneous medium with the same average dielectric constant. Accordingly, we obtain a very long dwell time for an incident plane wave even in a relatively thin film of photonic crystal. Figures 9(c) and 9(d) show the square of the norm of the total electric and the real part Poynting vector in the four periods-thick photonic crystal for incident plane waves corresponding to the previous Bloch modes. The direction of the Poynting vector points towards increasing values of  $x$  in both cases. The group velocity also points in the direction opposite to the Bloch vector. Clearly, the incident incident plane waves are coupled to resonant PIR modes in both the cases. In summary, modulating the radius of circular rods arranged in a square lattice to form a simple 3D cubic PC enables multiple PIR resonances. This leads to the enhancement of the short

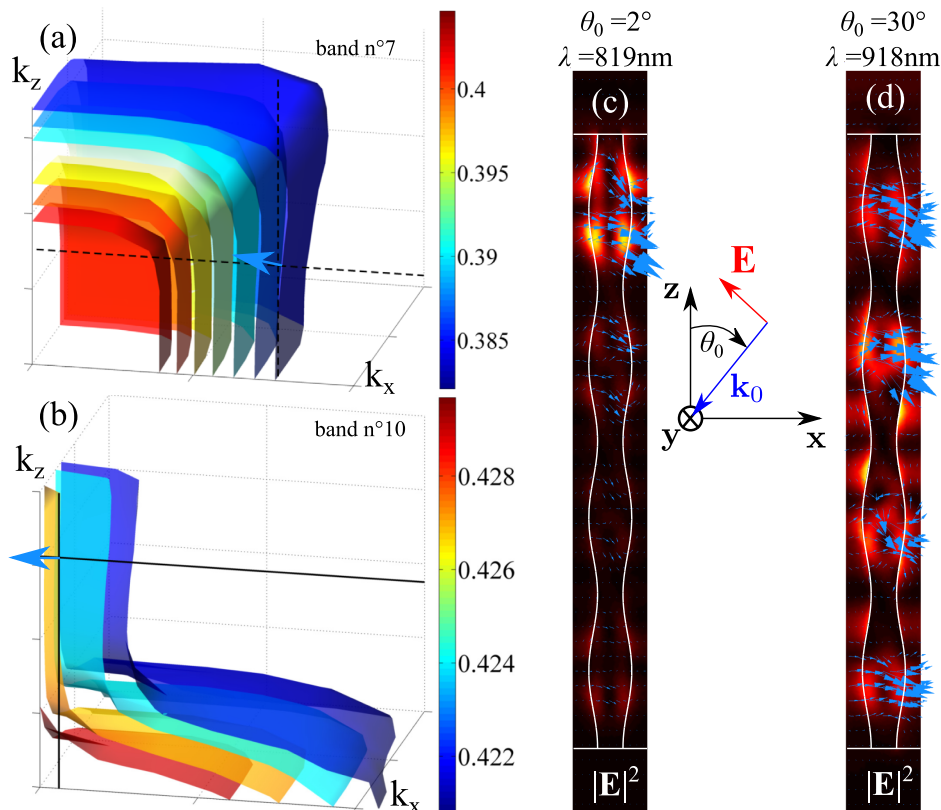


FIG. 9. PIR effect from band 7 and 10. (a) Iso-frequency surfaces of band 7. The blue arrow corresponds to the group velocity at  $\mathbf{k}$ -point  $(0.383 \frac{\pi}{a_x}, 0, 0.382 \frac{\pi}{a_z})$ . It lies in the  $x - y$  plane. (b) Iso-frequency surfaces of band 10. The blue arrow corresponds to the group velocity at  $\mathbf{k}$ -point  $(0.030 \frac{\pi}{a_x}, 0, 0.782 \frac{\pi}{a_z})$ . It also lies in the  $x - y$  plane. (c) Cut in plane  $x - z$  showing the square norm of the electric field and Poynting vector distributions in the photonic crystal slab of 4 unit cells thick. The incident plane wave is defined by  $(\lambda, \theta_0, \varphi_0, \psi_0) = (819 \text{ nm}, 2^\circ, 0^\circ, 0^\circ)$  so that the transverse components of the wave-vector match the transverse components of the Bloch vector at  $\mathbf{k}$ -point  $(0.030 \frac{\pi}{a_x}, 0, 0.782 \frac{\pi}{a_z})$ . The Poynting vector predominantly points towards the direction parallel to the interfaces of the PC slab with air, consistent with the direction of the group velocity found in (b). (d) Cut in  $x - z$  plane showing the square norm of the electric field (normalized to the incident intensity) and Poynting vector distributions in the same photonic crystal slab with incident plane wave defined by  $(\lambda, \theta_0, \varphi_0, \psi_0) = (918 \text{ nm}, 30^\circ, 0^\circ, 0^\circ)$ . Here the transverse components of the wavevector match the transverse components of the Bloch vector at  $\mathbf{k}$ -point  $(0.383 \frac{\pi}{a_x}, 0, 0.382 \frac{\pi}{a_z})$ . The Poynting vector direction is again parallel to the interfaces, consistent with the group velocity direction found in (a). In both cases there is strong light intensity focussing at particular positions in the PIR resonance modes. Peak intensity enhancement factors are approximately 150 relative to the incident plane wave.

circuit current  $J_{750}^{\lambda_s}$  by trapping light into slow modes propagating parallel to the interfaces of the slab. The performance of this light trapping scheme is compared to another recently proposed photonic crystal solar cell architecture in Sec. V.

## V. COMPARISON WITH OTHER ULTRA-THIN PHOTONIC CRYSTAL NANOSTRUCTURE

An alternative ultra-thin film diffractive solar architecture was recently proposed by Mallick *et al.*<sup>21</sup> As depicted in Fig. 10(a), this square lattice photonic crystal consists, along the direction of propagation of light, of (i) a 70 nm thick patterned silicon nitride antireflective layer, (ii) two stacked concentric nano-hole arrays in silicon of same period 600 nm but different diameters corresponding to an equivalent bulk thickness of 211 nm, (iii) a 400 nm thick silicon dioxide spacer, and (iv) a silver back-reflector. The optical performance of this device was retrieved using our finite element scheme and formalism described in Sec. II, and the values found in Ref. 41 for the optical constants of materials. The short circuit current at normal incidence is found to be  $J_{400}^{\lambda_s}(0,0,0) = 18.95 \text{ mA/cm}^2$ , instead of the  $21.8 \text{ mA/cm}^2$  claimed by the authors. We find that 4.6% of the usable solar spectrum [400 nm–1200 nm] is lost by absorption in the silver back-reflector. 42% of the solar power is absorbed in the silicon region and is available to produce photocurrent, and the remainder is reflected.

The physical explanation of this high solar absorption with such little silicon lies in the strong coupling of incident light to modes of the waveguides formed by the two nano-holes arrays. This coupling is strongly enhanced by the presence of the silver back-reflector. Indeed, the light trapping scheme relies on the ability of this structure to deflect an incident k-vector into off-normal non-zero diffraction orders that travel into the spacer. The diffracted light is then reflected by the silver back-reflector and finally coupled into the guided modes of the silicon nano-hole slabs. Without any back-reflector, i.e., considering the stacked nano-holes array lying on a semi-infinite substrate of silicon dioxide, the short circuit current at normal incidence drops to  $12.04 \text{ mA/cm}^2$ . This is still substantial given that the equivalent bulk thickness of

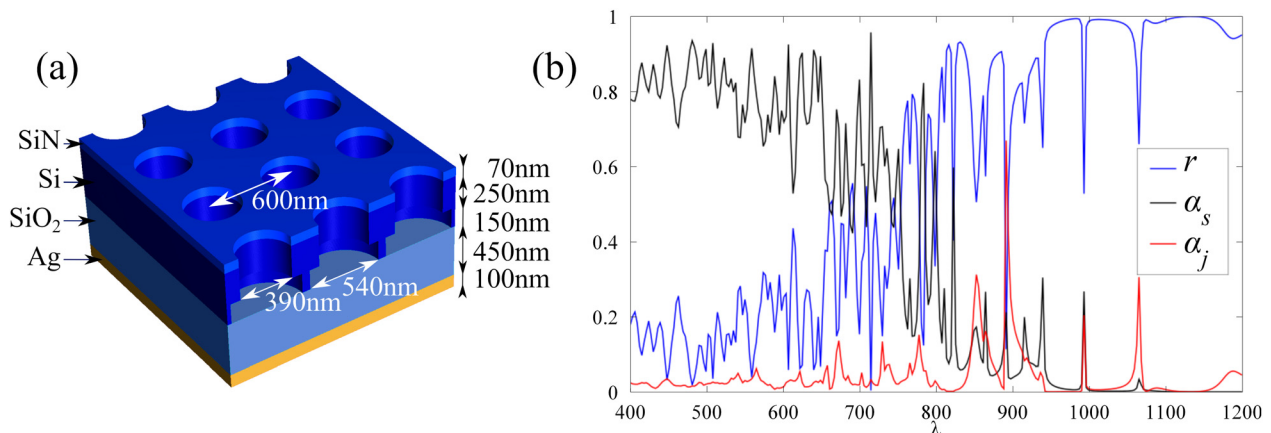


FIG. 10. (a) Solar cell device studied in Ref. 21, after final optimization. It consists of two stacked arrays of nano-holes of different diameter in silicon, a silicon dioxide spacer, a silver back-reflector, and a patterned silicon nitride antireflection coating. (b) Reflection spectrum  $r$  (in blue), Joules losses  $\alpha_j$  in the silver back-reflector (in red), and optical absorption in silicon  $\alpha_s$  (in black).

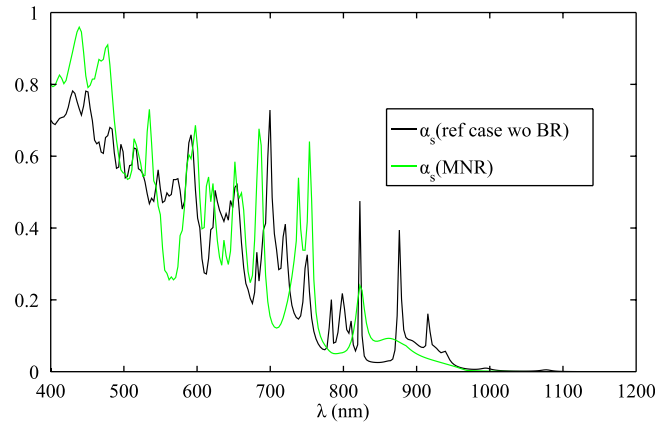


FIG. 11. Absorption spectrum (black curve) of the reference case<sup>21</sup> after replacing silver back-reflector with quartz substrate ( $J_{400}^{1200} = 12.04 \text{ mA/cm}^2$ ). In green, absorption spectrum of the modulated nanowires array using the same equivalent thickness of silicon (211 nm) as in the reference case ( $J_{400}^{1200} = 12.56 \text{ mA/cm}^2$ ).

silicon is only 211 nm. A modulated silicon nanowires array (embedded in  $\text{SiO}_2$ ) with the same equivalent bulk thickness of 211 nm, but with no silicon nitride antireflection layer and with modulation parameters  $(a, a_z, r_0, r_m) = (350, 310, 0.233, 0.05)$ , has a slightly stronger short circuit current at normal incidence of  $12.56 \text{ mA/cm}^2$ . The absorption spectrum of the structure in Ref. 21 without any silver back-reflector and the absorption spectrum of the MN array with  $(a, a_z, r_0, r_m) = (350, 310, 0.233, 0.05)$  are represented in Fig. 11 in black and green, respectively. Even in the absence of any antireflection layer or back-reflector, our modulated silicon nanowire array, operating purely with the parallel-to-interface refraction mechanism for light trapping, is competitive with state-of-the-art architectures.

## VI. BACK-REFLECTION WITH CHIRPED PHOTONIC CRYSTAL MIRROR

As detailed in Sec. IV, a strong modulation of the radii of the nanowires creates wide 1-D stop gaps in the photonic band structure of the modulated nanowires. Consequently, strong modulation in the base of the nanowire can be used

for broadband back-reflection. As suggested in Fig. 5, the spectral range of reflection can be tuned with  $a_z$  or other parameters. In this section, a chirped modulation is introduced in order to enlarge the bandwidth of back-reflection. We consider two families of chirped modulated nanowires. One consists of a chirped vertical periodicity while keeping  $(a, r_0, r_m) = (350, 0.233, 0.12)$  constant. The vertical periodicity  $a_z$  varies linearly with  $z$  from 243 nm to 500 nm. The other family of chirped modulated nanowires exhibits a chirped mean radius  $r_0$  while keeping  $(a, a_z, r_m) = (350, 300, 0.06)$  constant. The radius varies linearly with  $z$  from  $0.2a$  to  $0.43a$ . Both structures are represented in Figs. 12(a) and 12(b) and are referred as  $a_z$ -CMNBR and  $r_0$ -CMNBR ( $a_z$ -/ $r_0$ -chirped

modulated nanowire back-reflector). They both are placed just below the best PIR light trapping and absorbing configuration  $(a, a_z, r_0, r_m) = (350, 730, 0.233, 0.06)$  found in Sec. IV, denoted MN as previously.

First, the back-reflection performance of the two chirped structures is analyzed solely, i.e., without any MN structure above. An incident plane wave enters these chirped structures until it meets the period corresponding to a stop-gap for its wavelength, where it is reflected. Since this back-reflector (BR) is made of silicon, it not only prevents transmission but also contributes to a high absorption. As shown in Fig. 12(c) in blue, the  $r_0$ -chirped structure presents very low transmission in the visible range. The transmission  $t(\lambda)$  remains

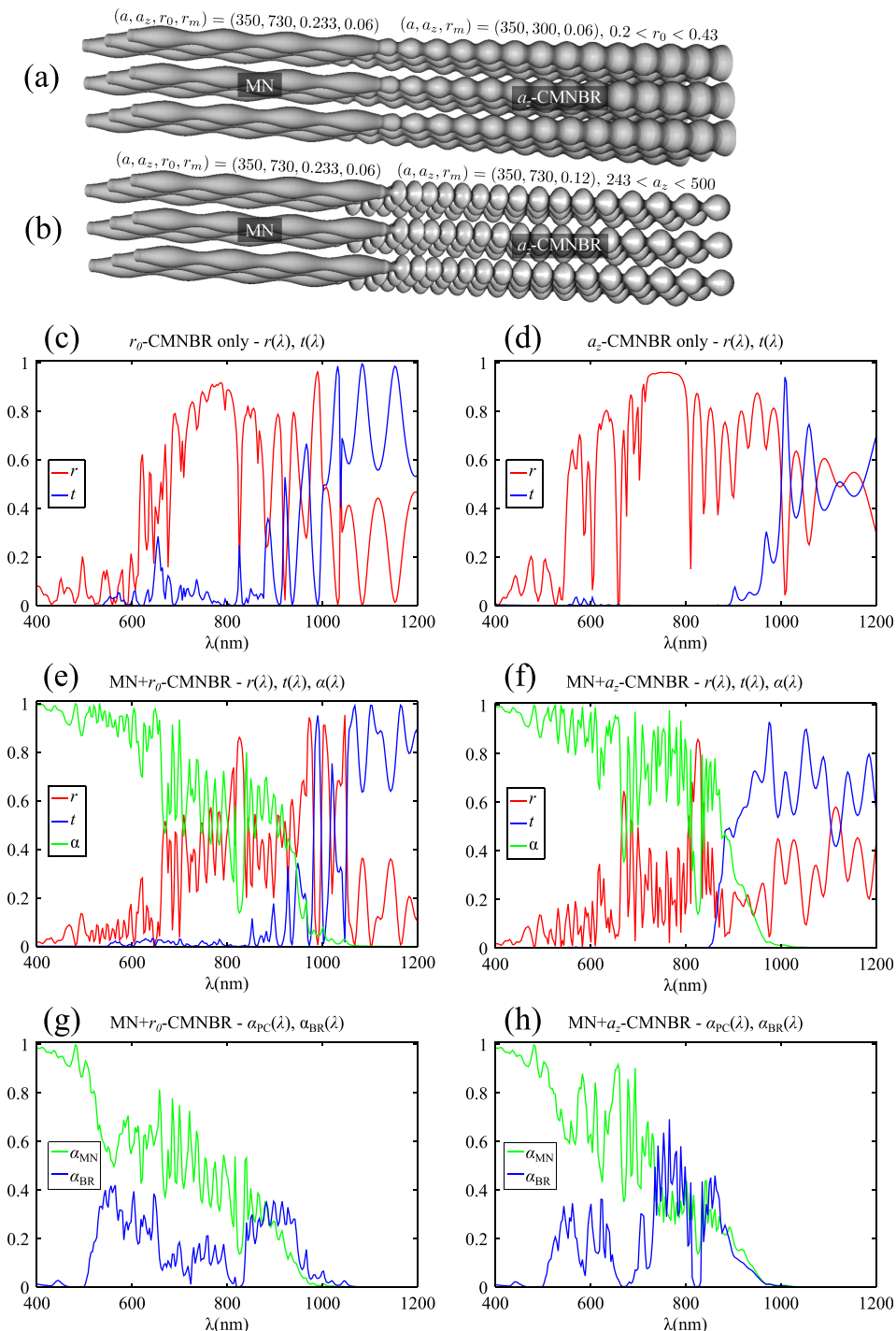


FIG. 12. (a) Photonic crystal  $(a, a_z, r_0, r_m) = (350, 730, 0.233, 0.06)$  and back reflector (BR) made of modulated nanowires with a chirped radius. (b) Photonic crystal  $(a, a_z, r_0, r_m) = (350, 730, 0.233, 0.06)$  and back reflector made of modulated nanowires with a chirped vertical periodicity. (c),(d) Reflection and transmission spectra of the two BR structures alone. All silicon structures are embedded in silicon dioxide up to the air boundary and seated on a quartz substrate.

lower than 3.5% from 400 nm to 897 nm, the rest of the incident field being either reflected or absorbed. In this spectral range [400 nm–897 nm] and at normal incidence, the fractions of incident power reflected, absorbed, and transmitted are, respectively,  $R_{400}^{897}(0, 0, 0) = 54\%$ ,  $A_{400}^{897}(0, 0, 0) = 45.7\%$ , and  $T_{400}^{897}(0, 0, 0) = 0.3\%$ . As depicted in Fig. 12(d), the  $a_z$ -chirped architecture is less reflective, but more absorptive than the  $r_0$ -chirped one. In the spectral range [400 nm–897 nm] and at normal incidence, the fractions of incident power reflected, absorbed, and transmitted are, respectively,  $R_{400}^{897}(0, 0, 0) = 42\%$ ,  $A_{400}^{897}(0, 0, 0) = 53.5\%$ , and  $T_{400}^{897}(0, 0, 0) = 4.5\%$ .

The tandem configuration consisting of CMNBR structures placed below the MN structure is next analyzed. We first observe that the short-circuit current  $J_{400}^{\lambda_s}(0, 0, 0) = 17.39 \text{ mA/cm}^2$  of the MN structure alone placed directly on a quartz substrate is less than the short circuit current  $J_{400}^{\lambda_s}(0, 0, 0) = 21.40 \text{ mA/cm}^2$  of the MN structure placed directly on a silver substrate. In other words, a bulk silver back-reflector would enhance the  $J_{400}^{\lambda_s}(0, 0, 0)$  of the MN configuration by 23%. However, 6.6% of the incident power in the spectral range [400 nm–1200 nm] is lost to Joule heat in the silver BR.

The performance of any chirped modulated nanowire BR alone is worse than that of a silver BR in terms of pure back-reflection into the MN structure. Indeed, light penetrates the BR to a significant depth, resulting in higher absorption and lower reflectivity. However, the fundamental difference from a silver layer is that absorption in the CMNBR structure made of silicon can ultimately participate in the photocurrent, whereas the power dissipated by Joule heat inside the silver BR is wasted.

The configuration MN +  $a_z$ -CMNBR (resp. MN +  $r_0$ -CMNBR) leads to an overall  $J_{400}^{\lambda_s}(0, 0, 0) = 25.81 \text{ mA/cm}^2$  (resp.  $25.19 \text{ mA/cm}^2$ ). Both structures are encased in SiO<sub>2</sub>, sit on a quartz substrate, and have an equivalent bulk thickness of 1942 and 1338 nm, respectively. The top MN structure has a contribution of  $19.39 \text{ mA/cm}^2$  (resp.  $19.16 \text{ mA/cm}^2$ ) to this value. It means that the  $a_z$ -CMNBR (resp.  $r_0$ -CMNBR) enhances the contribution of the MN segment to the short circuit current by 11.5% (resp. 10.2%). This is less than the 23% enhancement due to a silver layer back-reflector. Nevertheless these CMNBR structures serve as

dielectric back-reflector by increasing the absorption inside the MN segment above them. More importantly, they provide supplementary electron-hole pairs ultimately participating to the photocurrent, from photons at wavelengths that were previously transmitted by the MN structure. Reflection, transmission, and absorption spectra of the MN +  $a_z$ -CMNBR (resp. MN +  $r_0$ -CMNBR) structure are represented in Fig. 12(f) (resp. Fig. 12(e)). The individual contributions of the MN structure and the  $a_z$ -CMNBR structure (resp.  $r_0$ -CMNBR) to the total absorption spectrum are elucidated in Fig. 12(h) (resp. Fig. 12(g)). For the tandem structures described above, a rather long Bragg reflector (involving a large amount of silicon) was considered for illustrative purposes. As we show later, a much shorter dielectric mirror segment can produce almost the same maximum achievable photo-current density in an overall structure with about only  $1 \mu\text{m}$  of equivalent bulk thickness of silicon.

From a purely numerical point of view, MN +  $a_z$ -CMNBR leads to a slightly higher short circuit current of  $25.81 \text{ mA/cm}^2$  using a smaller amount of material. From an experimental point of view, the MN +  $r_0$ -CMNBR is more stable since the basis of each pillar is thicker. Also, the modulation amplitude  $r_m$  of the MN +  $r_0$ -CMNBR is weaker than that of the MN +  $a_z$ -CMNBR structure (0.06 instead of 0.12).

## VII. ANTIREFLECTION NANOCONES

For the structures considered above, sunlight traverses directly from air into a high refractive index photonic crystal consisting of silicon nano-rods embedded in SiO<sub>2</sub>. Consequently, a considerable amount of sunlight undergoes specular reflection at the air to solid interface. Considerable improvement in solar absorption can be realized using a graded effective index of refraction rather than a large abrupt change in the index. An effective graded-index profile can be obtained, for instance, using subwavelength arrays of nanocones. Their anti-reflection properties have been intensively studied both numerically and experimentally.<sup>22</sup> Recently antireflective properties of such conical coatings were studied in a whole range of size-to-wavelength ratios, including effective medium and geometric optics regimes.<sup>11</sup>

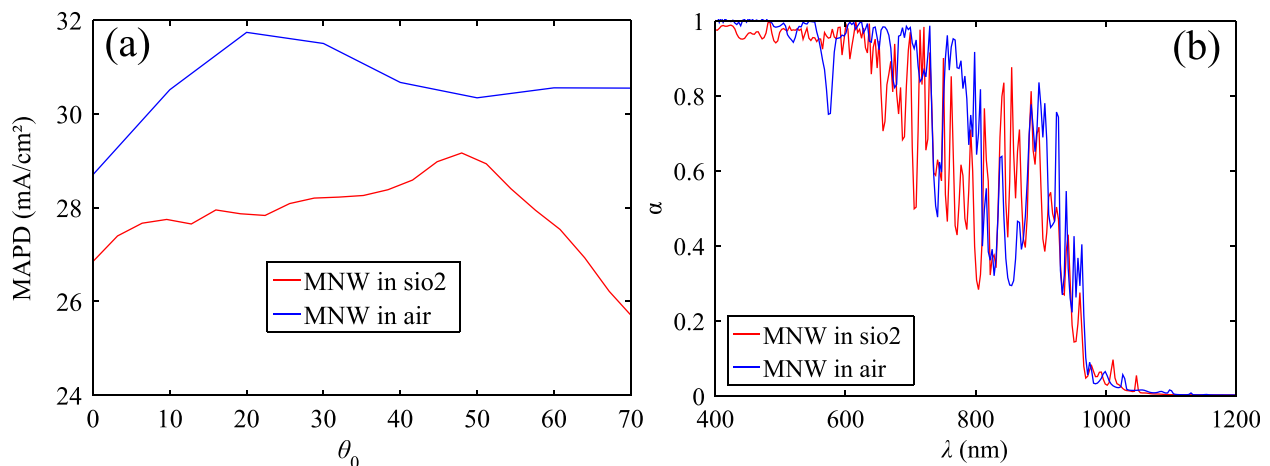


FIG. 13. Comparison of overall absorption (as measured by MAPD) for modulated nanowires embedded in SiO<sub>2</sub> (red curves) and embedded in air (blue curve), seated on a quartz substrate. (a) MAPD vs incident angle  $\theta_0$  for  $p$ -polarized light. (b) Optical absorption coefficient vs. wavelength. Roughly 15% improvement in MAPD is found for nanowires in air instead of SiO<sub>2</sub>.

For practical purposes, the MN +  $r_0$ -CMNBR structure is considered in what follows. A linear modulation of the radius  $r_0$  of nanowires leads to the formation of nanocones at the top of each modulated nanowire as shown in Fig. 15. We consider a specific illustration where the height of each nanocone is chosen to be 1385 nm. This slight gradation of the average refractive index with depth provides an anti-reflective (AR) effect. Indeed, the overall reflectivity at normal incidence  $R_{400}^{\lambda_{sg}}(0, 0, 0)$  drops from 28.4% to 24.5% when adding this AR coating at the top of the MN +  $r_0$ -CMNBR configuration. The overall reflection is still relatively large since the silicon nanocones are embedded in the SiO<sub>2</sub> background, which presents a sudden jump in the refractive index at the air to solid interface. In addition to the resulting specular reflection, substantial reflection is caused by the chirped Bragg mirror segment at the bottom of the nanowire.

From the electronic perspective, the very thin tips of the nanocones may be useful in harnessing “hot” electrons (with energy far above the bottom of the electronic conduction band of silicon) before they have had time to lose energy by thermalization processes. This thermalization is the cause of loss of approximately one-third of electrical power from incoming sunlight. By placing electrical contacts sufficiently close to the point of hot carrier generation, it may be possible to harness this additional power. Indeed, a large fraction of the high energy (blue-green) solar spectrum is absorbed in the nanocone segment of our silicon nanowires. For charge carrier separation and collection, a radial P-N junction is ideal.

For the configuration AR + MN +  $r_0$ -CMNBR, the short circuit current is enhanced to  $J_{400}^{\lambda_{sg}}(0, 0, 0) = 27.17$  mA/cm<sup>2</sup>. This is an additional 7.9% enhancement compared to the previous case without any AR shaping. This result is obtained using a SiO<sub>2</sub> background that fills all interstitial regions

between the silicon nanowires and which forms a flat surface at the tip of the nanocones. Considerable further improvement is likely if the SiO<sub>2</sub>-air boundary is itself modulated to provide a more gradual increase in the average refractive index with depth.

The equivalent bulk slab thickness of silicon of the MN +  $r_0$ -CMNBR structure described above is 1943 nm, whereas equivalent silicon slab thickness of the MN photonic crystal segment is only 500 nm. Clearly, the back-reflector segment consists of a very large amount of semi-conductor material. The height of the chirped modulated pillars forming the back-reflector alone is now 3.92  $\mu$ m. Our numerical studies reveal that the similar performance can be obtained using a much smaller amount of silicon for the back-reflector. Indeed, with only four periods ( $a_z = 300$  nm) of the  $r_0$ -chirped modulation for the back-reflector (that is a height of 1.2  $\mu$ m instead of 3.92  $\mu$ m), the short circuit current becomes  $J_{400}^{\lambda_{sg}}(0, 0, 0) = 25.94$  mA/cm<sup>2</sup> instead of 27.17 mA/cm<sup>2</sup>. In other words, reducing the back-reflector thickness by 47% in the amount of silicon used and the equivalent bulk slab thickness of the entire structure from 1943 nm to 1040 nm weakens the performance of the device by only 4.5% (1.23 mA/cm<sup>2</sup>). This modified nanowire profile is depicted in Fig. 14(c).

In summary, modulation of the radius of the classical nanowires to form a 3D simple cubic PC slab exhibits a broad-band parallel-to-interface refraction effect, leading to an enhanced light trapping and absorption. Adding a dielectric back-reflector based on a chirped modulation of the radius of the nanowire improves solar absorption in the light trapping region above and provides supplementary PIR effects at longer wavelength. Adding an antireflective nanostructure at the top consisting of nanocones improves absorption in the blue region of the spectrum and creates a reservoir

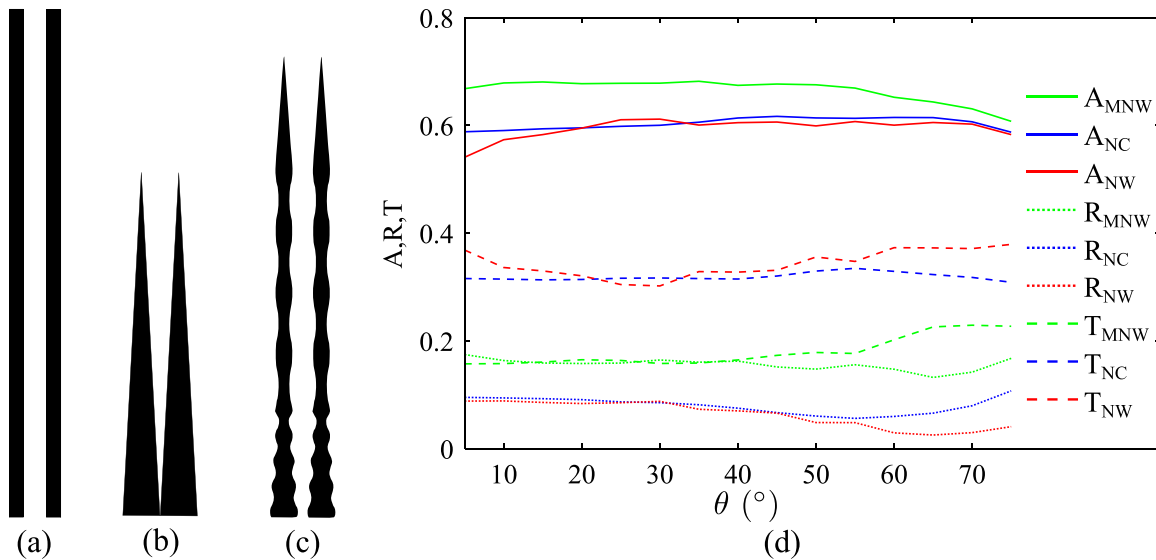


FIG. 14. The optimized MNW photonic crystal with a shorter BR (c) found in Sec. VII is compared to other photonic crystal nano-structures such as nanowires (NW), (a), nanocones (NC), (b). Cross sections in the  $x$ - $z$  plane of two adjacent unit cells are depicted. Proportions are respected in the insets (a), (b), and (c). The lattice constants  $a_x$  and  $a_y$  are set to 350 nm for all three architectures. The height of each nano-structure (a),(b) is adjusted so that their respective equivalent bulk slab thickness remains equal to the one of the optimized MNW structure (1040 nm). A 1040-nm-thick bulk slab made of crystalline silicon leads to a short circuit current  $J_{400}^{\lambda_{sg}}(0^\circ, 0^\circ, 0^\circ) = 8.8$  mA/cm<sup>2</sup>, the optimized nanowire array (a) to  $J_{400}^{\lambda_{sg}}(0^\circ, 0^\circ, 0^\circ) = 20.7$  mA/cm<sup>2</sup>, the optimized nanocone array (b) to  $J_{400}^{\lambda_{sg}}(0^\circ, 0^\circ, 0^\circ) = 22.1$  mA/cm<sup>2</sup>, and the optimized MNW (c) to  $J_{400}^{\lambda_{sg}}(0^\circ, 0^\circ, 0^\circ) = 25.9$  mA/cm<sup>2</sup>. In (d), the integrated absorption  $A_{400}^{\lambda_{sg}}(\theta, 0^\circ, 0^\circ)$ , reflection  $R_{400}^{\lambda_{sg}}(\theta, 0^\circ, 0^\circ)$ , and transmission  $T_{400}^{\lambda_{sg}}(\theta, 0^\circ, 0^\circ)$  are represented, respectively, by solid, small dashed, and large dashed lines, respectively. The following color code is used: green lines depict results for the MNW, blue those of the NC, and red those of the straight NW.

of “hottest” electrons localized within a confined volume within the tip of the nanocone. The antireflective nanocones also act as a coupler for incident light in free space into PIR modes at longer wavelength.

### VIII. COMPARISON WITH OTHER NANOWIRE ARCHITECTURES

In this section, we compare the solar absorption of our optimized modulated photonic crystal with other optimized unmodulated nanowires or nanocones with the same equivalent bulk thickness (1040 nm) of silicon. This comparison accentuates the significance of the high density of sharp optical resonances associated with parallel interface refraction. For the 2D photonic crystal of straight-walled nanowires, the parameters used are optimized for maximum absorption as detailed in Sec. III, i.e.,  $a_x = a_y = 350$  nm and  $r_0 = 0.233$ , while their height is adjusted to produce an equivalent bulk thickness of 1040 nm, i.e.,  $h = 6075$  nm. As a second reference case, we consider a 2D square lattice of pure nanocones (see Fig. 14(b)) of silicon. The nanocones shape is optimized to provide maximum solar absorption. The geometry of the nanocones slab is described by  $a_x = a_y = 350$  nm while the radius linearly decreases from  $r_0 = 0.49$  at the bottom of the

rod to  $r_0 = 0$  at the top of the structure. The height of the nanocone is set to  $h = 4132$  nm so that the equivalent bulk silicon thickness is 1040 nm. Figs. 14(a) and 14(b) show cross sections in the plane (xOz) or (yOz) of two lattice constants of the conventional nanowires and nanocones, respectively. Fig. 14(c) depicts the optimized architecture found in Sec. VII with a reduced thinner  $r_0$ -chirped modulated back-reflector.

For comparison, we note that a simple unstructured 1040-nm-thick slab of silicon resting on a quartz substrate leads to a short circuit current under normal illumination of  $J_{400}^{\lambda_{gs}}(0^\circ, 0^\circ, 0^\circ) = 8.8$  mA/cm<sup>2</sup>. Shaping this semi-conductor material into an optimized 2D PC of straight-walled conventional nanowires leads to a 235% enhancement with short circuit current of  $J_{400}^{\lambda_{gs}}(0^\circ, 0^\circ, 0^\circ) = 20.7$  mA/cm<sup>2</sup>. A simple but optimized modulation of the wire radius along the vertical direction to form nanocones (see Fig. 14(b)) leads to a short circuit current  $J_{400}^{\lambda_{gs}}(0^\circ, 0^\circ, 0^\circ) = 22.1$  mA/cm<sup>2</sup>. This is an additional 6.8% enhancement. Finally, our proposed MNR structure (Fig. 14(c)) with a short circuit current  $J_{400}^{\lambda_{gs}}(0^\circ, 0^\circ, 0^\circ) = 25.9$  mA/cm<sup>2</sup> represents a 17.2% further enhancement compared to the nanocones. This enhancement is due to the parallel-to-interface refraction light trapping mechanism.

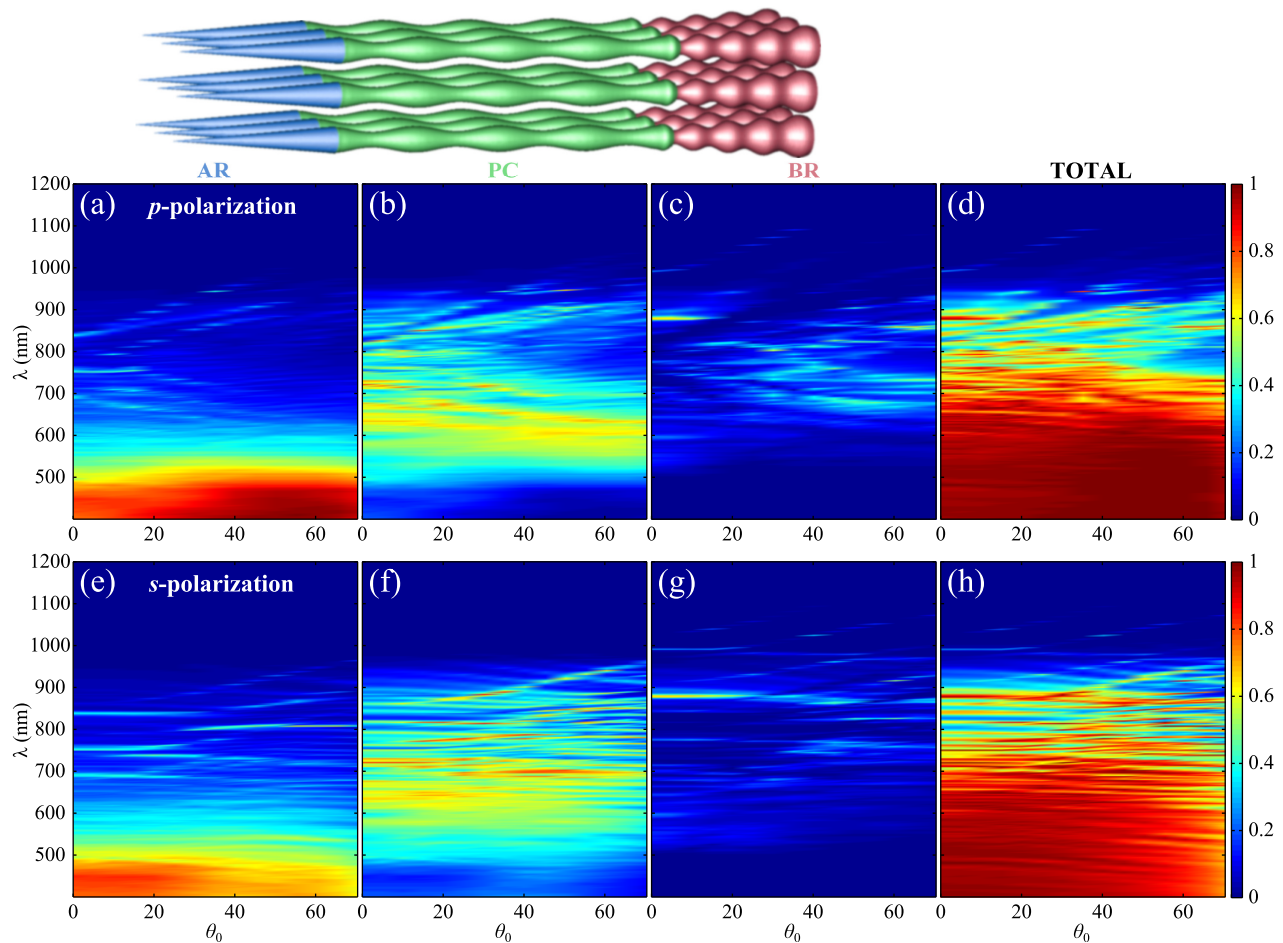


FIG. 15. Detailed angular and polarization-resolved absorption characteristics of the AR + MN +  $r_0$ -CMNR structure. The value of unity (dark red) corresponds to 100% absorption of sunlight at a particular wavelength  $\lambda$  and incident angle  $\theta_0$ . The total absorption  $\alpha(\lambda, \theta_0, 0^\circ, 0^\circ)$  (resp.  $\alpha(\lambda, \theta_0, 0^\circ, 90^\circ)$ ) is presented in (d) (resp. (h)) as a color map in the  $p$ -polarization (resp.  $s$ -polarization) case. The fraction of total absorption occurring in the AR region is detailed in (a) (resp. (e)), in the MN region in (b) (resp. (f)), in the  $r_0$ -CMNR region in (c) (resp. (g)).

In general we find that for thin film (with equivalent bulk thickness of silicon of about one micron or less) the sinusoidally modulated nanowires with PIR outperforms other architectures with the same amount of silicon. For the case of thicker films (with much more than one micron equivalent bulk thickness of silicon), there are a number of competing architectures with comparable performance.

## IX. ANGULAR RESPONSE OF SIMPLE CUBIC NANOWIRE PHOTONIC CRYSTAL

Among the most noteworthy characteristics of the sinusoidally modulated nanowire photonic crystal is its exceptionally good performance over a broad range of incident angles (from zero to  $80^\circ$  relative to the normal).

In this section, the role of each segment of the composite structure AR + MN +  $r_0$ -CMNBR (depicted at the top of Fig. 15) is analyzed by calculating the angular response of the total device. We show that each segment of the nanowire targets absorption in separate parts of the solar spectrum presented on Fig. 1.

Absorption at shorter wavelengths [400 nm–500 nm] is specifically achieved by the antireflective nanocones at the top of each nanowire (depicted in blue on the sketch of Fig. 15). These nanocones perform two main functions. First, they enable excellent absorption in this spectral range, over a broad range [ $0^\circ$ ,  $70^\circ$ ,] of incident angles  $\theta_0$  for both  $s$  and  $p$ -polarization, as shown in Figs. 15(a) and 15(e). These high energy photons generate “hot” carriers in a small volume at the tip of each cone. The collection of these hot electrons prior to thermalization can significantly enhance the electrical efficiency of solar cells. Second, the nanocones enhance the coupling of longer wavelength photons from free space to the lower segments of the nanowire array. In the middle wavelength range [500 nm–900 nm], light trapping and absorption is facilitated by a high density of sharp PIR resonances in the simple cubic 3D photonic crystal directly underneath the nanocones. These resonances cover a broad range of wavelengths and can be activated from a wide range of incident angles. This is depicted in Figs. 15(b) and 15(f). Enhanced absorption is due to the flatness of several photonic bands and associated “slow light” as detailed in Sec. IV. The optical absorption in this segment of the photonic crystal (MN) also benefits from the broadband back-reflection provided by the  $r_0$ -CMNBR photonic crystal placed directly underneath. At wavelengths close to the electronic band gap of silicon [900 nm–1100 nm], the  $r_0$ -CMNBR structure becomes the main absorber, as shown in Figs. 15(c) and 15(g). The resonances here can be attributed to parallel to interface refraction as well.

## X. COMPOSITIONAL MODULATION $\text{Si}_x\text{Ge}_{1-x}$ IN BRAGG MIRROR

While the 3-segment nanowire photonic crystal described in previous sections are effective in trapping and absorbing sunlight of wavelengths shorter than 1000 nm, a substantial fraction (nearly 20%) of the solar power consists of photons with energy below the electronic band gap of crystalline silicon. Long wavelength light of this nature is

neither trapped effectively nor absorbed in a purely silicon nanowire. Traditional multi-junction solar cells<sup>44</sup> attempt to harness this broader spectrum of light by stacking in series different semiconductor materials with sequentially lower electronic band gaps. In this section, we consider an additional compositional chirp of the structurally chirped Bragg mirror segment at the bottom of each nanowire. This has a two-fold effect. On the electronic side, it causes a continuous shift of the electronic band gap from that of silicon at the top of the chirped Bragg mirror section of the nanowire to that of germanium at the bottom. On the optical point of view, it provides a wider frequency shift (with depth in the nanowire) of the 1D photonic stop gap. The larger refractive index of germanium allows a broader range of frequencies to experience back-reflection by the chirped dielectric mirror. The expanded absorption spectrum of the doubly chirped nanowire leads to a significant increase in the maximum achievable photo-current density. In this paper, we do not consider strategies to optimize the open circuit voltage and the overall efficiency of the resulting solar cell.

The structure referred to as AR + MN +  $r_0$ -CMNBR (equivalent bulk thickness of 1943 nm) shows good performance for photons of energy greater than the 1.124 eV, the electronic band gap of silicon. In order to extend its performance to the near infrared, we consider a compositional chirp using silicon-germanium  $\text{Si}_x\text{Ge}_{1-x}$  alloys in the base section of our nanowire solar cell.

In particular, we consider the AR + MN +  $r_0$ -CMNBR long nanowire structure (equivalent bulk thickness of 1943 nm) embedded in silicon dioxide and replace the silicon  $r_0$ -CMNBR back-reflector by the alloy  $\text{Si}_x\text{Ge}_{1-x}$ , keeping the same geometric properties. The graded index profile is numerically implemented along the 3923 nm height of the chirped back-reflector segment as follows. This height is divided into eleven slices of 357 nm each so that the upper slice is made of pure silicon ( $x=0$ ) and the lower slice is made of pure germanium ( $x=1$ ). The  $n$ -th slice, counting from the top, is then made of  $\text{Si}_{1-n/10}\text{Ge}_{n/10}$  for  $n \in \{0, 1, 2, 3, 4, 5, 6, 7, 8, 9, 10\}$ . A smoothing polynomial function is applied between two slices and the thickness of the transition between two slices is set to 100 nm.

The absorption spectra at normal incidence of individual nanowire segments,  $\alpha_{\text{AR}}$  (in blue),  $\alpha_{\text{MN}}$  (in green), and  $\alpha_{\text{BR}}$  (in red), of the AR + MN +  $r_0$ -CMNBR structure are depicted in Fig. 16, together with (in black) the total absorption spectrum. Replacing the Si back-reflector with a  $\text{Si}_x\text{Ge}_{1-x}$  alloy back-reflector increases the short circuit current density  $J_{400}^{1800}(0^\circ, 0^\circ, 0^\circ)$  from 27.17 mA/cm<sup>2</sup> to 33.79 mA/cm<sup>2</sup>. This is a 24.4% enhancement in solar absorption. The contribution from the antireflective nanocones to the overall absorption of light is 30%, whereas the middle section of modulated nanowires contributes 39% and the graded-index back-reflector contributes 31%. It is likely that a modification of the compositional profile to include a region of pure germanium would enable additional absorption peaks at wavelengths longer than 1.6  $\mu\text{m}$ . However, a strategy is required to prevent the flow of carriers generated in silicon-rich regions into the germanium-rich regions where the open circuit voltage across the P-N junction is considerably less than that in pure silicon. Such a

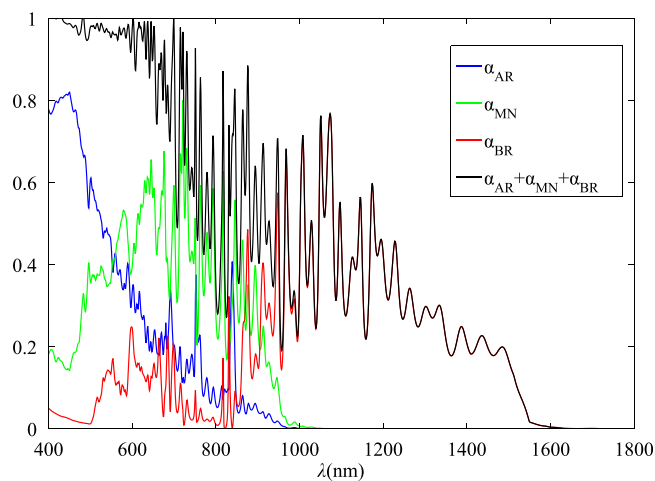


FIG. 16. Absorption spectra at normal incidence for AR + MN +  $r_0$ -CMNBR structure, where  $r_0$ -CMNBR has a  $\text{Si}_x\text{Ge}_{1-x}$  graded index profile in depth. The contribution to the total absorption (in black) from the antireflective nanocones ( $\alpha_{\text{AR}}$ ) is represented in blue, the one from the PIR modulated nanowire ( $\alpha_{\text{MN}}$ ) in green, and the one from the  $\text{Si}_x\text{Ge}_{1-x}$  graded index back-reflector ( $\alpha_{\text{BR}}$ ) in red. The resulting short current density  $J_{400}^{1800}(0^\circ, 0^\circ, 0^\circ)$  is  $33.79 \text{ mA/cm}^2$ : 30% coming from the nanocones, 39% coming from the PIR modulated nanowires, 31% coming from the  $\text{Si}_x\text{Ge}_{1-x}$  graded index back-reflector. The nanowire photonic crystal is embedded in  $\text{SiO}_2$  and sits on a quartz substrate.

short circuit path for the photo-current would seriously reduce the power efficiency of the solar cell.

## XI. CONCLUDING REMARKS

In summary, we have illustrated a specific design, based on modulated nanowires, of a 3-D, thin-film, simple cubic photonic crystal exhibiting solar light trapping. This particular design enables absorption of 75% of all available sunlight in the 400 nm–1200 nm spectral range, from nearly any angle of incidence, using only one micron of equivalent bulk thickness of crystalline silicon. It would be of considerable interest to compare this solar absorption characteristic to other 3D simple cubic photonic crystal exhibiting strong parallel to interface refraction. These include modulated pore designs,<sup>31</sup> simple cubic woodpiles,<sup>45</sup> and slanted pore photonic crystals.<sup>46</sup> These alternative light-trapping architectures may require different P-N junction geometries, unlike the radial P-N junction proposed for our nanowire array.

Our modulated nanowire arrays are all packaged in a silicon dioxide matrix that fills all the interstitial regions between the nanowires up to the tip of the nanocones. The resulting flat-top  $\text{SiO}_2$ -air boundary at the tip of the nanocones leads to considerable reflection of sunlight. In the absence of this  $\text{SiO}_2$  matrix, the MAPD are improved by approximately 15% (see Fig. 13). A similar gain in short circuit current density is expected with an improved antireflection strategy near the top of our nanowires.

Our structure absorbs 75% of sunlight in the 400 nm–1200 nm range without recourse to any metallic mirror at the base of the nanowire array. The addition of a metallic mirror would add to the cost of the structure and add only slight improvement in the MAPD. Another important consideration is the optical response of the metallic contacts placed around

each nanowire to collect the generated photocurrent. Such contacts may improve light focussing and absorption characteristics, but some part of the additional absorbed energy may be lost to Joule heating in the contact.

To estimate the overall power efficiency of the modulated nanowire photonic crystal solar cell, it is important to couple the solution of Maxwell's equations to the semiconductor drift-diffusion equations<sup>47,48</sup> governing the charge carrier transport within the nanowire. Given our overall light absorption, typical non-radiative recombination losses, and open-circuit voltages in the silicon solar cells, we anticipate an overall power efficiency in the range of 15%–20% (Ref. 47) in our photonic crystal with only one micron of equivalent bulk thickness of silicon. Although our nanowires involve a large amount of surface area, the surface recombination velocity at the Si– $\text{SiO}_2$  surface is typically in the range of 100–1000 cm/s.<sup>49,50</sup> Employing a modulated radial P-N junction geometry that efficiently separates charge carriers, the solution of the semiconductor drift-diffusion equations demonstrates minor recombination at the Si– $\text{SiO}_2$  boundary.<sup>47</sup> The majority of nonradiative recombination occurs near metallic contacts where the corresponding surface recombination velocity is several orders of magnitude larger. A 15%–20% power efficiency would be a significant improvement relative to commercial silicon solar cells employing 300 microns in thickness of unstructured silicon. This estimate is based on the assumption of instantaneous thermalization of photo-generated carriers. On the other hand, a substantial fraction of electron-hole pairs in our nanowire array are generated in the nanocone section of the wire. With a suitably placed contact, such carriers may only need to drift tens of nanometers, with incomplete thermalization prior to collection. Such “hot carrier” collection would improve further the overall power efficiency of the solar cell.

In a silicon solar cell, roughly 19% of the incident solar power is lost due to photons of energy below the indirect electronic band gap of silicon. Our simple illustration of using a Si-Ge alloy at the base of the nanowires to absorb these low energy photons comes at the cost of a substantial drop in the operating voltage of the solar cell. Alternatively, it may be possible to up-convert these low-energy photons using non-linear effects in the glass matrix surrounding the nanowires. This may be achieved by doping the glass matrix with rare earth ions<sup>8–10</sup> that cause a pair of low energy photons to combine and be up-converted to a single high energy photon above the electronic band gap of silicon. This type of non linear process may be greatly enhanced by the high-intensity focussing of light and the slow group-velocity modes of the photonic crystal optical resonances. A combination of a solar concentrator, above the nanowire array, with factor of 150 light intensity enhancement in certain regions due to photonic crystal focussing effects may have dramatic consequences for reshaping of the solar spectrum in the silicon nanowires for enhanced power efficiency.

In conclusion, thin-film photonic crystals solar cells offer a number of important opportunities for enhanced photonic and electronic management in nano-structured photovoltaic devices. These include light trapping over a broad spectral and angular range, spectral reshaping of the solar

spectrum, and “hot carrier” collection, all within a single integrated nano-structure. While our discussion has focussed on silicon solar cells, similar considerations may apply to other materials, such as GaAs, CdTe, organic, and dye-sensitized TiO<sub>2</sub> devices.

## ACKNOWLEDGMENTS

This work was supported in part by the United States Department of Energy Contract DE-FG02-10ER46754, the Natural Sciences and Engineering Research Council of Canada, and the Canadian Institute for Advanced Research.

- <sup>1</sup>C. Gueymard, D. Myers, and K. Emery, “Proposed reference irradiance spectra for solar energy systems testing,” *Sol. Energy* **73**(6), 443–467 (2002).
- <sup>2</sup>M. Green, “Thin-film solar cells: Review of materials, technologies and commercial status,” *J. Mater. Sci.: Mater. Electron.* **18**, 15–19 (2007).
- <sup>3</sup>K. Catchpole and A. Polman, “Plasmonic solar cells,” *Opt. Express* **16**(26), 21793–21800 (2008).
- <sup>4</sup>M. Green, *Third Generation Photovoltaics: Advanced Solar Energy Conversion* (Springer-Verlag, 2003).
- <sup>5</sup>G. Conibeer, R. Patterson, L. Huang, J. Guillemoles, D. König, S. Shrestha, and M. Green, “Modelling of hot carrier solar cell absorbers,” *Sol. Energy Mater. Sol. Cells* **94**(9), 1516–1521 (2010).
- <sup>6</sup>P. Aliberti, Y. Feng, Y. Takeda, S. Shrestha, M. Green, and G. Conibeer, “Investigation of theoretical efficiency limit of hot carriers solar cells with a bulk indium nitride absorber,” *J. Appl. Phys.* **108**, 094507 (2010).
- <sup>7</sup>D. König, K. Casalenuovo, Y. Takeda, G. Conibeer, J. Guillemoles, R. Patterson, L. Huang, and M. Green, “Hot carrier solar cells: Principles, materials and design,” *Phys. E: Low-Dimens. Syst. Nanostruct.* **42**(10), 2862–2866 (2010).
- <sup>8</sup>T. Trupke, M. Green, and P. Würfel, “Improving solar cell efficiencies by up-conversion of sub-band-gap light,” *J. Appl. Phys.* **92**, 4117 (2002).
- <sup>9</sup>B. Richards and A. Shalav, “Enhancing the near-infrared spectral response of silicon optoelectronic devices via up-conversion,” *IEEE Trans. Electron Devices* **54**(10), 2679–2684 (2007).
- <sup>10</sup>A. Shalav, B. Richards, and M. Green, “Luminescent layers for enhanced silicon solar cell performance: Up-conversion,” *Sol. Energy Mater. Sol. Cells* **91**(9), 829–842 (2007).
- <sup>11</sup>A. Deinega, I. Valuev, B. Potapkin, and Y. Lozovik, “Minimizing light reflection from dielectric textured surface,” *J. Opt. Soc. Am. A* **28**(5), 770–777 (2011).
- <sup>12</sup>S. John, “Electromagnetic absorption in a disordered medium near a photon mobility edge,” *Phys. Rev. Lett.* **53**(22), 2169–2172 (1984).
- <sup>13</sup>S. John, “Strong localization of photons in certain disordered dielectric superlattices,” *Phys. Rev. Lett.* **58**(23), 2486–2489 (1987).
- <sup>14</sup>G. Lozano, S. Colodrero, O. Caulier, M. E. Calvo, and H. Miguez, “Theoretical analysis of the performance of one-dimensional photonic crystal-based dye-sensitized solar cells,” *J. Phys. Chem. C* **114**(8), 3681–3687 (2010).
- <sup>15</sup>P. Bermel, C. Luo, L. Zeng, L. C. Kimerling, and J. D. Joannopoulos, “Improving thin-film crystalline silicon solar cell efficiencies with photonic crystals,” *Opt. Express* **15**(25), 16986–17000 (2007).
- <sup>16</sup>P. G. O’Brien, A. Chutinan, K. Leong, N. P. Kherani, G. A. Ozin, and S. Zukotynski, “Photonic crystal intermediate reflectors for micromorph solar cells: A comparative study,” *Opt. Express* **18**(5), 4478–4490 (2010).
- <sup>17</sup>J. G. Mutitu, S. Shi, C. Chen, T. Creazzo, A. Barnett, C. Honsberg, and D. W. Prather, “Thin film solar cell design based on photonic crystal and diffractive grating structures,” *Opt. Express* **16**(19), 15238–15248 (2008).
- <sup>18</sup>J. Üpping, A. Bielawny, P. Miclea, and R. Wehrspohn, “3D photonic crystals for ultra-light trapping in solar cells,” *Proc. SPIE* **7002**, 23 (2008).
- <sup>19</sup>T. Suezaki, P. O’Brien, J. Chen, E. Loso, N. Kherani, and G. Ozin, “Tailoring the electrical properties of inverse silicon opals – A step towards optically amplified silicon solar cells,” *Adv. Mater.* **21**(5), 559–563 (2009).
- <sup>20</sup>Y. Song, J. Yu, and Y. Lee, “Antireflective submicrometer gratings on thin-film silicon solar cells for light-absorption enhancement,” *Opt. Lett.* **35**(3), 276–278 (2010).
- <sup>21</sup>S. Mallick, M. Agrawal, and P. Peumans, “Optimal light trapping in ultra-thin photonic crystal crystalline silicon solar cells,” *Opt. Express* **18**(6), 5691–5706 (2010).
- <sup>22</sup>J. Zhu, Z. Yu, G. F. Burkhard, C.-M. Hsu, S. T. Connor, Y. Xu, Q. Wang, M. McGehee, S. Fan, and Y. Cui, “Optical absorption enhancement in amorphous silicon nanowire and nanocone arrays,” *Nano Lett.* **9**(1), 279–282 (2009).
- <sup>23</sup>B. Kayes, H. Atwater, and N. Lewis, “Comparison of the device physics principles of planar and radial pn junction nanorod solar cells,” *J. Appl. Phys.* **97**(11), 114302–114302 (2005).
- <sup>24</sup>M. D. Kelzenberg, S. W. Boettcher, J. A. Petykiewicz, D. B. Turner-Evans, M. C. Putnam, E. L. Warren, J.M. Spurgeon, R. M. Briggs, N. S. Lewis, and H. A. Atwater, “Enhanced absorption and carrier collection in Si wire arrays for photovoltaic applications,” *Nat. Mater.* **9**(3), 239–244 (2010).
- <sup>25</sup>B. Tian, X. Zheng, T. Kempa, Y. Fang, N. Yu, G. Yu, J. Huang, and C. Lieber, “Coaxial silicon nanowires as solar cells and nanoelectronic power sources,” *Nature (London)* **449**(7164), 885–889 (2007).
- <sup>26</sup>J. Li, H. Yu, S. Wong, G. Zhang, X. Sun, P. Lo, and D. Kwong, “Si nanopillar array optimization on Si thin films for solar energy harvesting,” *Appl. Phys. Lett.* **95**, 033102 (2009).
- <sup>27</sup>V. Sivakov, G. Andrä, A. Gawlik, A. Berger, J. Plentz, F. Falk, and S. Christiansen, “Silicon nanowire-based solar cells on glass: Synthesis, optical properties, and cell parameters,” *Nano Lett.* **9**(4), 1549–1554 (2009).
- <sup>28</sup>E. Garnett and P. Yang, “Light trapping in silicon nanowire solar cells,” *Nano Lett.* **10**(3), 1082–1087 (2010).
- <sup>29</sup>L. Hu and G. Chen, “Analysis of optical absorption in silicon nanowire arrays for photovoltaic applications,” *Nano Lett.* **7**(11), 3249–3252 (2007).
- <sup>30</sup>N. Lagos, M. M. Sigalas, and D. Niarchos, “The optical absorption of nanowire arrays,” *Photonics Nanostruct. Fundam. Appl.* **9**(2), 163–167 (2011).
- <sup>31</sup>A. Chutinan and S. John, “Light trapping and absorption optimization in certain thin-film photonic crystal architectures,” *Phys. Rev. A* **78**, 023825 (2008).
- <sup>32</sup>R. Petit, L. Botten *et al.*, *Electromagnetic Theory of Gratings* (Springer-Verlag, Berlin, 1980), Vol. 62.
- <sup>33</sup>G. Demésy, F. Zolla, A. Nicolet, and M. Commandré, “Versatile full-vectorial finite element model for crossed gratings,” *Opt. Lett.* **34**(14), 2216–2218 (2009).
- <sup>34</sup>G. Demésy, F. Zolla, A. Nicolet, and M. Commandré, “All-purpose finite element formulation for arbitrarily shaped crossed-gratings embedded in a multilayered stack,” *J. Opt. Soc. Am. A* **27**, 878–889 (2010).
- <sup>35</sup>A. Taflov and S. H. Hagness, *Computational Electrodynamics: The Finite Difference Time-Domain Method* (Artech House, 2005).
- <sup>36</sup>A. Deinega and I. Valuev, “Subpixel smoothing for conductive and dispersive media in the FDTD method,” *Opt. Lett.* **32**, 3429–3431 (2007).
- <sup>37</sup>I. Valuev, A. Deinega, and S. Belousov, “Iterative technique for analysis of periodic structures at oblique incidence in the finite-difference time-domain method,” *Opt. Lett.* **33**, 1491–1493 (2008).
- <sup>38</sup>A. Deinega and S. John, “Effective optical response of silicon to sunlight in the finite-difference time-domain method,” *Opt. Lett.* **37**, 112–114 (2012).
- <sup>39</sup>W. Shockley and H. Queisser, “Detailed balance limit of efficiency of p-n junction solar cells,” *J. Appl. Phys.* **32**, 510 (1961).
- <sup>40</sup>See <http://rredc.nrel.gov/solar/spectra/am1.5/> for reference numerical data about the solar spectrum.
- <sup>41</sup>E. Palik and G. Ghosh, *Handbook of Optical Constants of Solids: Five-Volume Set* (Academic, 1998).
- <sup>42</sup>A. Nicolet, S. Guenneau, C. Geuzaine, and F. Zolla, “Modeling of electromagnetic waves in periodic media with finite elements,” *J. Comput. Appl. Math.* **168**, 321–329 (2004).
- <sup>43</sup>O. Toader and S. John, “Photonic band gap enhancement in frequency-dependent dielectrics,” *Phys. Rev. E* **70**(4), 046605 (2004).
- <sup>44</sup>R. King, D. Law, K. Edmondson, C. Fetzer, G. Kinsey, H. Yoon, R. Sherif, and N. Karam, “40% efficient metamorphic gainp/gainas/ge multijunction solar cells,” *Appl. Phys. Lett.* **90**(18), 183516–183516 (2007).
- <sup>45</sup>N. Tétéault, G. von Freymann, M. Deubel, M. Hermatschweiler, F. Pérez-Willard, S. John, M. Wegener, and G. Ozin, “New route to three-dimensional photonic bandgap materials: Silicon double inversion of polymer templates,” *Adv. Mater.* **18**(4), 457–460 (2006).
- <sup>46</sup>O. Toader and S. John, “Slanted-pore photonic band-gap materials,” *Phys. Rev. E* **71**(3), 036605 (2005).
- <sup>47</sup>A. Deinega and S. John, “Solar power conversion efficiency in modulated silicon nanowire photonic crystals,” *J. Appl. Phys.* **112**, 074327 (2012).
- <sup>48</sup>A. Deinega and S. John, “Finite difference discretization of semiconductor drift-diffusion equations for nanowire solar cells,” *Comp. Phys. Comm.* **183**, 2128 (2012).
- <sup>49</sup>M. D. Kelzenberg, D. B. Turner-Evans, B. M. Kayes, A. Michael, M. C. Putnam, N. S. Lewis, and H. A. Atwater, “Photovoltaic measurements in single-nanowire silicon solar cells,” *Nano Lett.* **8**(2), 710–714 (2008).
- <sup>50</sup>M. A. Green, *Silicon Solar Cells: Advanced Principles & Practice* (Centre for Photovoltaic Devices and Systems, University of New South Wales, 1995).